



EC-Earth3-AerChem, a global climate model with interactive aerosols and atmospheric chemistry participating in CMIP6

5 Twan van Noije¹, Tommi Bergman^{1,2}, Philippe Le Sager¹, Declan O'Donnell², Risto Makkonen^{2,3}, María Gonçalves-Ageitos^{4,5}, Ralf Döscher⁶, Uwe Fladrich⁶, Jost von Hardenberg⁷, Jukka-Pekka Keskinen^{2,3},
Hannele Korhonen², Anton Laakso⁸, Stelios Myriokefalitakis⁹, Pirkka Ollinaho², Carlos Pérez García-Pando^{4,10}, Thomas Reerink¹, Roland Schrödner^{11,*}, Klaus Wyser⁶, and Shuting Yang¹²

¹Royal Netherlands Meteorological Institute, De Bilt, Netherlands

²Climate System Research, Finnish Meteorological Institute, Helsinki, Finland

³Institute for Atmospheric and Earth System Research, Faculty of Science, University of Helsinki, Helsinki, Finland

10 ⁴Barcelona Supercomputing Center, Barcelona, Spain

⁵Technical University of Catalonia, Barcelona, Spain

⁶Swedish Meteorological and Hydrological Institute, Norrköping, Sweden

⁷Institute of Atmospheric Sciences and Climate, National Research Council, Turin, Italy

⁸Atmospheric Research Centre of Eastern Finland, Finnish Meteorological Institute, Kuopio, Finland

15 ⁹Institute for Environmental Research and Sustainable Development, National Observatory of Athens, Athens, Greece

¹⁰ICREA, Catalan Institution for Research and Advanced Studies, Barcelona, Spain

¹¹Centre for Environmental and Climate Research, Lund University, Lund, Sweden

¹²Danish Meteorological Institute, Copenhagen, Denmark

*now at: Leibniz Institute for Tropospheric Research, Leipzig, Germany

20 *Correspondence to:* Twan van Noije (noije@knmi.nl)

Abstract. This paper documents the global climate model EC-Earth3-AerChem, one of the members of the EC-Earth3 family of models participating in the Coupled Model Intercomparison Project phase 6 (CMIP6). EC-Earth3-AerChem has interactive aerosols and atmospheric chemistry and contributes to the Aerosols and Chemistry Model Intercomparison Project (AerChemMIP). In this paper, we give an overview of the model and describe in detail how it differs from the other EC-Earth3 configurations, and what the new features are compared to the previously documented version of the model (EC-Earth 2.4). We explain how the model was tuned and spun up under pre-industrial conditions and characterize the model's general performance on the basis of a selection of coupled simulations conducted for CMIP6. The mean energy imbalance at the top of the atmosphere in the pre-industrial control simulation is $-0.10 \pm 0.25 \text{ W m}^{-2}$ and shows no significant drift. The corresponding mean global surface air temperature is $14.05 \pm 0.16 \text{ }^\circ\text{C}$, with a small drift of $-0.075 \pm 0.009 \text{ }^\circ\text{C per century}$. The model's effective equilibrium climate sensitivity is estimated at $3.9 \text{ }^\circ\text{C}$ and its transient climate response at $2.1 \text{ }^\circ\text{C}$. The CMIP6 historical simulation displays spurious interdecadal variability in Northern Hemisphere temperatures, resulting in a large spread among ensemble members and a tendency to underestimate observed annual surface temperature anomalies from the early 20th century onwards. The observed warming of the Southern Hemisphere is well reproduced by the model. Compared to the ERA5 reanalysis of the European Centre for Medium-Range Weather Forecasts, the ensemble mean surface air temperature climatology for 1995–2014 has an average bias of $-0.86 \pm 0.35 \text{ }^\circ\text{C}$ in the Northern Hemisphere and $1.29 \pm 0.05 \text{ }^\circ\text{C}$ in the Southern Hemisphere. The Southern Hemisphere warm bias is largely caused by errors in shortwave cloud radiative effects over the Southern Ocean, a deficiency of many climate models. Changes in the emissions of near-term climate forcers (NTCFs) have significant climate effects from the 20th century onwards. For the SSP3-7.0 shared socio-economic pathway, the model gives a global warming at the end of the 21st century (2091–2100) of $4.9 \text{ }^\circ\text{C}$ above the pre-industrial mean. A $0.5 \text{ }^\circ\text{C}$ stronger warming is obtained for the AerChemMIP scenario with reduced emissions of NTCFs. With concurrent reductions of future methane concentrations, the warming is projected to be reduced by $0.5 \text{ }^\circ\text{C}$.



1 Introduction

EC-Earth is a global climate and Earth system model developed by a European consortium of meteorological services, research institutes, and high-performance computing centres (Hazeleger et al., 2010; 2012). Activities in recent years were dedicated to the development of the third generation of the model and participation in the Coupled Model Intercomparison Project phase 6 (CMIP6; Eyring et al., 2016). The basic CMIP6 configuration of the model (EC-Earth version 3.3.1.1, hereafter referred to as EC-Earth3) consists of an atmospheric general circulation model (GCM) based on cycle 36r4 of the Integrated Forecasting System (IFS) from the European Centre for Medium-Range Weather Forecasts (ECMWF), coupled to the NEMO-LIM3 global ocean–sea ice model from the Nucleus for European Modelling of the Ocean (NEMO) release 3.6 (Rousset et al., 2015). Other CMIP6 configurations include additional modules for simulating dynamic vegetation, the carbon cycle, aerosols and atmospheric chemistry, or the Greenland ice sheet. Low- and high-resolution configurations have also been developed. An overview of the different configurations is given by Döscher et al. (in preparation). Specific model configurations will be documented in separate publications. This paper documents the configuration with interactive aerosols and atmospheric chemistry (EC-Earth-AerChem version 3.3.3, hereafter EC-Earth3-AerChem). It is with this configuration that the EC-Earth consortium participates in the Aerosols and Chemistry Model Intercomparison Project (AerChemMIP; Collins et al., 2017).

The distinguishing feature of EC-Earth3-AerChem compared to the other EC-Earth configurations applied in CMIP6, is that it simulates tropospheric aerosols and the reactive greenhouse gases methane and ozone. In all other configurations these are prescribed as described by Döscher et al. (in preparation). Although methane and stratospheric ozone are not fully prescribed in EC-Earth3-AerChem, they are constrained by the CMIP6 forcing data sets of Meinshausen et al. (2017; 2020) and Checa-Garcia et al. (2018), respectively. As a result, the main differences between EC-Earth3-AerChem and the other CMIP6 configurations of EC-Earth are related to tropospheric aerosols and tropospheric and lower-stratospheric ozone, and how they interact with the climate system.

In this paper we describe the model and present first results from CMIP6 simulations. The remainder of the paper is structured as follows. The model description is given in Sect. 2. In this section we subsequently describe the main general characteristics of the model as well as the treatment of aerosols and their interactions with radiation and clouds, atmospheric chemistry and chemical boundary conditions, and anthropogenic and natural emissions, and finally some relevant technical and numerical aspects of the model. The applied tuning and spin-up procedures are outlined in Sect. 3. Results from CMIP6 simulations are presented in Sect. 4. The analysis presented in this section focuses on the effective equilibrium climate sensitivity and the transient climate response, the net energy imbalance in the simulations, and the long-term evolution and present-day climatology of surface air temperatures. Finally, we end the paper with a discussion and conclusions in Sect. 5.

2 Model description

2.1 General

EC-Earth3-AerChem is essentially EC-Earth3 (Döscher et al., in preparation) extended with an additional component to simulate aerosols and atmospheric chemistry. The atmospheric GCM is based on IFS cycle 36r4, which includes the land surface model H-TESSEL (revised hydrology version of TESSEL, the Tiled ECMWF Scheme for Surface Exchanges over Land; Balsamo et al., 2009). Its horizontal resolution is T₁₂₅₅ (triangular truncation at wavenumber 255 in spectral space with a linear N128 reduced



80 Gaussian grid, corresponding to a spacing of about 80 km). The atmospheric grid consists of 91 layers in the vertical direction and has a model top at 0.01 hPa. The time step applied in IFS is 45 min.

85 The McRad radiation package of cycle 36r4 consists of a shortwave (SW) and longwave (LW) radiation scheme based on the Rapid Radiative Transfer Model for General Circulation Models (RRTMG), and uses the Monte Carlo Independent Column Approximation (McICA) to treat the radiative transfer in clouds (Morcrette et al., 2008). Clouds and large-scale precipitation are described by prognostic equations for cloud liquid water, cloud ice, rain, snow and a grid box fractional cloud cover.

90 Compared to the original model from IFS cycle 36r4, several adjustments and updates have been made in EC-Earth (Döscher et al., in preparation). These include the application of global mass fixers for dry air and humidity (Diamantakis and Flemming, 2014), a resolution-dependent parameterisation of non-orographic gravity wave drag (Davini et al., 2017), and a diagnostic convective closure, which is dependent on the convective available potential energy (Bechtold et al., 2014). Moreover, the Abdul-Razzak and Ghan (2000) cloud activation scheme has been introduced, and a dependence of the autoconversion efficiency on the cloud droplet number concentration (CDNC) has been added, following Rotstayn and Penner (2001). Details about the representation of aerosol-cloud interactions in EC-Earth3-AerChem are given in Sect. 2.2.

95 Moreover, CMIP6 forcings have been introduced. For EC-Earth3-AerChem, the CMIP6 forcings prescribed in IFS are the solar forcing (Matthes et al., 2017), well-mixed greenhouse gas concentrations (CO₂, N₂O, CFC-12, and CFC-11 equivalents; Meinshausen et al., 2017; 2020), and stratospheric aerosol radiative properties. Vegetation fields consistent with the CMIP6 land use forcing data sets (Hurtt et al., 2020), which have been produced using a model configuration with dynamic vegetation (EC-Earth3-Veg), replace the climatological input fields applied in the standard IFS model. The corresponding surface albedo of the soil and vegetation is calculated as described by Döscher et al. (in preparation).

100 The ocean GCM is based on NEMO-LIM3 release 3.6 (Rousset et al., 2015), which consists of the Océan Parallélisé (OPA) ocean dynamics and thermodynamics model (Madec and the NEMO team, 2015) and the Louvain-la-Neuve sea ice model version 3 (LIM3; Vancoppenolle et al., 2009). Its horizontal grid is the tripolar ORCA1 grid, which has a resolution of approximately 1° with meridional refinement down to 1/3° in the tropics (Madec and Imbard, 1996; Hewitt et al., 2011). The ocean grid consists of 75 layers. The time step applied in NEMO is 45 min. Compared to the reference version from the release, a few modifications have been made in EC-Earth, as described by Döscher et al. (in preparation): turbulent kinetic energy is not allowed to penetrate below the ocean mixed layer, the strength of the Langmuir cell circulations has been increased, and the thermal conductivity of snow on sea ice has been slightly reduced.

110 IFS and NEMO are coupled by exchanging fields via OASIS3-MCT version 3.0 (Craig et al., 2017), a new version of the OASIS3 (Ocean Atmosphere Sea Ice Soil version 3) coupler interfaced with the Model Coupling Toolkit (MCT) from the Argonne National Laboratory. The discharge of continental freshwater into the oceans is described using a runoff mapper that instantaneously relocates the runoff from the interior of 66 major global drainage basins to the coast where it enters the ocean as freshwater. In a similar way, accumulated snow from the interior of the continents is removed and sent to the ocean as ice (“calving”) to prevent the snow from piling up where the temperature is low. The corresponding fields are passed from IFS to NEMO via the runoff mapper, which is coupled to the GCMs through OASIS.



120 In atmosphere-only simulations, NEMO and the runoff mapper are replaced by an interface (called AMIP reader in EC-Earth) that reads monthly or daily sea surface temperature and sea-ice concentration fields from a set of input files, applies temporal interpolation if needed, and sends daily fields to IFS via OASIS.

125 The setup of the couplings between IFS, NEMO and the runoff mapper or between IFS and the AMIP reader is the same in EC-Earth3-AerChem as in EC-Earth3. Also, the parameter settings adopted in these components are identical in both configurations, with the exception of three atmospheric parameters that have been slightly retuned (see Sect. 3).

130 Aerosols and atmospheric chemistry are simulated with the Tracer Model version 5 (TM5), specifically release 3.0 of the massively parallel version of TM5 (TM5-mp 3.0). It runs at a horizontal resolution of $3^\circ \times 2^\circ$ (longitude \times latitude) with 34 layers in the vertical direction. By origin, TM5 is a standalone atmospheric chemistry and transport model (CTM), which is driven by offline meteorological and surface fields (Krol et al., 2005; Huijnen et al., 2010). About a decade ago, TM5 was integrated as a module coupled to IFS within EC-Earth. A description and evaluation of the TM5-IFS coupled system in the previous generation of EC-Earth (version 2.4) was given by van Noije et al. (2014). Since then, the representation of chemistry and aerosols in TM5 has been revised in many respects, and interactions with radiation and clouds have been introduced. In the remainder of this section we will briefly describe how TM5 and relevant aspects in IFS have changed compared to the system documented in van Noije et al. (2014).

135

2.2 Aerosols and their interactions with radiation and clouds

140 The aerosol components represented in TM5 include sulfate (SO_4), black carbon (BC), organic aerosols (OA), sea salt, and mineral dust. These are described by the modal aerosol microphysical scheme M7 (Vignati et al., 2004), which consists of four water-soluble modes (nucleation, Aitken, accumulation, and coarse) and three insoluble modes (Aitken, accumulation and coarse). Particles inside the modes are assumed to be internally mixed. Each mode is described by a log-normal size distribution with a fixed geometric standard deviation. For each mode, M7 describes the evolution of the total particle number and mass of each species. The scheme accounts for new particle formation, water uptake, and ageing through coalescence and condensation.

145 Other aerosol components described by TM5 are ammonium (NH_4), nitrate (NO_3), methane sulfonic acid (MSA), and the diagnostic radioactive tracer lead-210 (^{210}Pb). The concentrations of ammonium, nitrate and water associated with (ammonium) nitrate are determined based on equilibrium gas/particle partitioning calculations using EQSAM (Metzger et al., 2002). Ammonium nitrate is assumed to be present only in the soluble accumulation mode. MSA is produced by oxidation of dimethyl sulfide (DMS) in the gas phase and is assumed to condense instantaneously onto existing soluble accumulation-mode particles. When calculating the mass, size and optical properties of these particles, the model accounts for the presence of ammonium nitrate and its associated water, as well as MSA.

150 Aerosol water uptake is calculated using a diagnostic estimate of the clear-sky relative humidity. In grid boxes where the relative humidity (RH) is lower than or equal to 90 %, the clear-sky RH is set equal to the all-sky value; where the RH exceeds 90 %, the clear-sky RH is calculated by assuming that the RH is the area weighted average of the cloudy-sky RH, which is set to 100 %, and the clear-sky RH, and applying a minimum value of 75 %. Water uptake by sulphate and sea salt is calculated as described by Vignati et al. (2004): for internal mixtures containing sea salt, the water uptake is calculated using the ZSR method (Zdanovskii, 1948; Stokes and Robinson, 1966); in the absence of sea salt, the water uptake associated with sulphate is calculated using the



parameterization from Zeleznik (1991); black carbon, organic matter and dust do not influence the water uptake. Additional water uptake in the presence of ammonium nitrate in the soluble accumulation mode is calculated using EQSAM.

160

The densities of the various aerosol components are given in Table 1. The densities of black carbon and organic aerosols have been reduced from 2.0 g cm^{-3} in EC-Earth 2.4 to 1.8 g cm^{-3} (Bond and Bergstrom, 2006; Bond et al., 2013) and 1.3 g cm^{-3} (Turpin and Lim, 2001; Cross et al., 2007; Schmid et al., 2009; Lee et al., 2010; Kuwata et al., 2012; Nakao et al., 2013), respectively. Particulate organic matter is still assumed to have a constant carbon content. It is expressed by the ratio of the total mass of OA particles to the mass of the carbon they contain. This ratio is used to convert emissions of primary organic aerosols (POA) expressed as organic carbon (OC) mass to OA mass. A value of 1.6 is adopted for all POA sources (Turpin and Lim, 2001; Reid et al., 2005; Aiken et al., 2008). Previously, this ratio was set to 1.4 (van Noije et al., 2014; Tsigaridis et al., 2014). For the same amount of carbon emitted into the atmosphere and corresponding particle size distribution, 14 % more OA mass and 76 % more OA particles are emitted in the current model version, as a result of the reduction in the assumed particle density and carbon content of organic aerosols. Similarly, 11 % more BC particles are emitted as a result of the reduction in the assumed particle density of black carbon.

165

170

Table 1. Physical properties for the various aerosol components included in the model. For properties that have been updated, the numbers between parentheses indicate the values used in the earlier TM5 and EC-Earth versions documented in van Noije et al. (2014).

	Density (g cm^{-3})	Refractive index at 550 nm	Hygroscopicity parameter
Sulfate			
Sulfuric acid (H_2SO_4)	1.841	$1.43 + 1.0 \times 10^{-8} i$	0.6
Sodium sulfate (Na_2SO_4)	2.68	Not used	0.95
Sodium bisulfate (NaHSO_4)	2.435	Not used	Not used
Black carbon (BC)			
Black carbon (BC)	1.8 (2.0)	$1.85 + 0.71 i$ ($1.75 + 0.44 i$)	0.0
Organic aerosols (OA)			
Primary organic aerosols (POA)			
Primary organic aerosols (POA)	1.3 (2.0)	$1.53 + 5.5 \times 10^{-3} i$	0.1
Secondary organic aerosols (SOA)			
Secondary organic aerosols (SOA)	1.3 (2.0)	$1.53 + 5.5 \times 10^{-3} i$	0.1
Sea salt			
Sea salt	2.165	$1.50 + 1.0 \times 10^{-8} i$	1.0
Mineral dust			
Mineral dust	2.65	$1.52 + 1.1 \times 10^{-3} i$	0.0
Ammonium nitrate			
Ammonium nitrate	1.73 (1.70)	$1.43 + 1.0 \times 10^{-8} i$	0.6
MSA			
MSA	1.48	$1.43 + 1.0 \times 10^{-8} i$	0.6
Water			
Water	1.0	$1.336 + 2.5 \times 10^{-9} i$	-

175

The representation of secondary organic aerosols (SOA) has been substantially revised. A scheme has been introduced to simulate the formation of SOA in the atmosphere in a simplified way (Bergman et al., in preparation). To separately track the SOA mass in the respective modes, the original M7 framework has been extended by adding an additional transported SOA tracer in the soluble



180 nucleation, accumulation, Aitken, and coarse mode as well as in the insoluble Aitken mode. Consistent with the original M7 model,
 SOA is not produced in the insoluble accumulation and coarse modes, which consist of mineral dust only. The properties of SOA
 are currently assumed to be the same as for primary organic aerosols (POA; see Table 1). In the new SOA scheme, isoprene and
 monoterpenes, emitted by vegetation or produced by biomass burning, are oxidized by reacting with the hydroxyl radical (OH) or
 ozone (O₃). This produces, with specified yields, either extremely low-volatility organic compounds (represented by a single non-
 185 transported tracer called ELVOC) or semi-volatile organic compounds (represented by SVOC). ELVOC can take part in new
 particle formation or condense onto existing particles. SVOC, on the other hand, is too volatile to contribute to new particle
 formation but does produce SOA via condensation. It is assumed that all produced ELVOC and SVOC are converted into SOA in
 a single model time step (see Sect. 2.5). Condensation of ELVOC takes place in the kinetic regime, where the rate of condensation
 is proportional to the available particle surface area. Thus, the amount of SOA produced by condensation of ELVOC is distributed
 190 across the relevant modes in proportion to the total surface of the particles they contain. In contrast, consistent with equilibrium
 partitioning theory, the SOA production from SVOC is distributed in proportion to the total mass of OA (i.e., POA and SOA)
 contained in the modes. Condensation of SVOC on nucleation-mode particles is thereby neglected.

Also, the representation of new particle formation has been revised (Bergman et al., in preparation). The original M7 scheme only
 195 accounts for particle formation through binary homogeneous nucleation of water and sulfuric acid (H₂SO₄) from the gas phase.
 The corresponding rate of nucleation and critical cluster size are calculated using a parameterization from Vehkamäki et al. (2002),
 which is based on classical nucleation theory. However, existing theories of binary homogeneous nucleation tend to overestimate
 the sensitivity to sulfuric acid concentrations, and are not able to reproduce nucleation events that take place in the planetary
 boundary layer, suggesting that other trace gases like organics and ammonia are also involved in the early growth process (e.g.,
 200 Weber et al., 1996; Jung et al., 2008; Sipilä et al., 2010; Kerminen et al., 2010; Paasonen et al., 2010). To enhance the nucleation
 in the boundary layer, a second nucleation mechanism has been added, which describes new particle formation in the presence of
 sulfuric acid and low-volatility organic compounds, represented by ELVOC. Following Riccobono et al. (2014), the corresponding
 rate of nucleation is expressed as a two-component power law, with a quadratic dependence on the ambient vapour concentration
 of sulfuric acid and a linear dependence on the ELVOC concentration. The subsequent growth of the freshly formed particles to 5
 205 nm as a result of the condensation of sulfuric acid and ELVOC is described following Kerminen and Kulmala (2002).

Table 2. Scavenging fractions for convective and stratiform in-cloud scavenging. The numbers between parentheses indicate the
 values used in the earlier TM5 and EC-Earth versions documented in van Noije et al. (2014). In those versions, the distinction
 between liquid, mixed and ice clouds is made based on the cloud liquid and ice water content, and the scavenging fraction for
 210 mixed clouds depends on their ratio.

	Stratiform in-cloud scavenging			Convective scavenging
	Liquid clouds	Mixed clouds	Ice clouds	
Soluble modes				
Nucleation	0.06 (0.0)	0.06	0.06 (0.0)	0.2 (1.0)
Aitken	0.25 (0.0)	0.06	0.06 (0.0)	0.6 (1.0)
Accumulation	0.85 (1.0)	0.06	0.06 (0.2)	0.99 (1.0)



Coarse	0.99 (1.0)	0.75	0.06 (0.2)	0.99 (1.0)
Insoluble modes				
Aitken	0.2 (0.0)	0.06	0.06 (0.0)	0.2 (1.0)
Accumulation	0.4 (0.0)	0.06	0.06 (0.0)	0.4 (1.0)
Coarse	0.4 (0.0)	0.4	0.06 (0.0)	0.4 (1.0)
Bulk components	0.85 (0.7)	0.06	0.0 (0.14)	0.99 (0.99)

Table 3. Number and mass scavenging coefficients (mm^{-1}) for stratiform below-cloud scavenging. The numbers between parentheses indicate the values used in the TM5 and EC-Earth versions documented in van Noije et al. (2014).

	Number	Mass
Soluble and insoluble modes		
Nucleation	$0.02 (5 \times 10^{-3})$	$2 \times 10^{-3} (5 \times 10^{-3})$
Aitken	$1 \times 10^{-3} (2 \times 10^{-3})$	$2 \times 10^{-4} (2 \times 10^{-3})$
Accumulation	$3 \times 10^{-4} (8 \times 10^{-3})$	$0.03 (8 \times 10^{-3})$
Coarse	0.3 (1.0)	0.7 (1.0)
Bulk components	$3 \times 10^{-4} (1.0)$	0.03 (1.0)

215

Moreover, wet deposition rates describing the removal of aerosols by clouds and precipitation have been revised, as indicated in Tables 2 and 3. Scavenging of aerosols by precipitation formation in convective and stratiform clouds is described using prescribed mode-dependent scavenging fractions (Croft et al., 2010), which for convective clouds are taken from Stier et al. (2005) and for stratiform clouds from Bourgeois and Bey (2011) (see Table 2). For stratiform clouds a distinction is made between liquid, mixed and ice clouds. Here it is assumed that clouds are liquid at temperatures above 0°C , ice below -35°C , and mixed in between. Below-cloud scavenging of aerosols by stratiform precipitation is described using prescribed scavenging coefficients for the particle number and mass in each mode (see Table 3). These coefficients have been estimated from results presented by Croft et al. (2009), obtained for a standard Marshall-Palmer rain droplet size distribution and a precipitation rate of 1 mm hr^{-1} . Because different coefficients are applied to particle number and mass, below-cloud scavenging shifts the size distributions of the modes: the nucleation and Aitken modes are shifted to larger sizes and the accumulation and coarse modes to smaller sizes. All scavenging processes act with the same rate on the bulk aerosol components (ammonium, nitrate, MSA, and lead-210) as on the other components contained in the soluble accumulation mode. As in earlier versions of the model, in-cloud and below-cloud scavenging by stratiform clouds is reduced by delaying the subgrid-scale mixing between cloudy and cloud-free regions (see Vignati et al., 2010b). The corresponding mixing timescale has been made dependent on the horizontal resolution; at the resolution applied in EC-Earth3-AerChem, it has been increased from 3 to 6 hours.

220

225

230

The calculation of the removal of aerosols by sedimentation and surface dry deposition follows the description given by van de Brugh et al. (2011). Also here, distinct rates are applied to the particle number and mass in each mode. Compared to the version



documented by van Noije et al. (2014), dry deposition and sedimentation of ammonium, nitrate and MSA have been added. These
235 are now removed at the same rate as the other components contained in the soluble accumulation mode.

The aerosols simulated by TM5 are tropospheric in the sense that they mainly originate from surface emissions and sources in the
troposphere. TM5 does not include emissions from explosive volcanoes, which may reach the stratosphere when the eruption is
sufficiently strong, or chemical processes that are specifically relevant for particle formation in the stratosphere, such as the
240 production of sulfuric acid by the oxidation of carbonyl sulfide (COS). TM5 does simulate the transport of particles across the
tropopause and in the stratosphere, but it cannot be assumed to provide accurate information on stratospheric aerosols. For this
reason, IFS does not make use of any aerosol data from TM5 at levels above the model tropopause. Instead, radiative effects of
stratospheric aerosols are accounted for in RRTMG_{sw} and RRTMG_{lw} using prescribed radiative properties from CMIP6. The
treatment of stratospheric aerosols and the calculation of the tropopause level in IFS are identical to the implementation in EC-
245 Earth3 (see Döscher et al., in preparation).

The calculation of aerosol optical properties in TM5 is based on Mie theory (van Noije et al., 2014). The extinction, single-
scattering albedo and asymmetry factor are calculated for each mode at a number of predefined wavelength values. Spectral
refractive indices of the various aerosol components are prescribed using input tables from three different sources. For modes
250 consisting of internally mixed particles, effective refractive indices are calculated using volume mixing rules derived from
effective-medium theory. Sulfate, organic aerosols, sea salt, ammonium nitrate, MSA, and water are treated as homogeneous
mixtures described by the Bruggeman mixing rule. When black carbon and/or dust are present in the mix, these are treated as
inclusions in a homogeneous background medium, using the Maxwell Garnett mixing rule.

255 The refractive indices of sulfate and sea salt are from the OPAC package (Optical Properties of Aerosols and Clouds; Hess et al.,
1998). The values for sulfate were obtained for a solution consisting of 75 % H₂SO₄ in water. The volume occupied by sulfate is
calculated in the optics module of TM5 by assuming that all sulfate is present in the form of sulfuric acid. The refractive indices
of MSA and ammonium nitrate are assumed to be the same as for sulfate. For black carbon, the refractive index is prescribed using
the corresponding input table from OPAC but with the real and imaginary parts scaled by 1.85/1.75 and 0.71/0.44, respectively.
260 By applying these scale factors, the refractive index at 550 nm is changed from the OPAC value of $1.75 + 0.44 i$, used in previous
versions of the model, to $1.85 + 0.71 i$, i.e. the mid-range value proposed by Bond and Bergstrom (2006). The refractive indices of
organic aerosols and mineral dust are taken from the aerosol-climate model ECHAM-HAM (see Zhang et al., 2012). For OA the
values are based on OPAC; for dust the imaginary part in the visible part of the spectrum is much lower than in OPAC. The
refractive index of water is taken from Segelstein (1981). The corresponding values at 550 nm are given in Table 1.

265 The resulting aerosol optical properties are input to the photolysis scheme of TM5 (see Sect. 2.3) and the shortwave radiation
scheme of IFS (RRTMG_{sw}). Within each spectral band, the optical properties are calculated at a single wavelength value. For the
photolysis scheme, these are the ‘central’ wavelength values defined within the scheme. For RRTMG_{sw}, they are solar-weighted
band averages, with the solar spectral irradiance distribution acting as the weighting function. The corresponding wavelength
270 values are 257, 313, 398, 530, 697, 973, 1269, 1447, 1767, 2040, 2308, 2752, 3407, 5254 nm. For diagnostic purposes, the optical
properties are also determined at a limited number of additional wavelengths (440, 550, and 870 nm). In accordance with the
CMIP6 data request, the contributions from the stratosphere are not included in the output optical property fields.



275 Absorption of longwave radiation by tropospheric aerosols is included in RRTM_{GLW} using a simplified approach that makes use
of pre-computed mass attenuation coefficients (MACs) from the prognostic aerosol scheme developed in IFS by Morcrette et al.
(2009). The aerosol components represented in this scheme are sulfate, black carbon, organic aerosols, sea salt and mineral dust.
For black carbon and organic aerosols, the hydrophobic and hydrophilic components are treated separately. Sea salt and dust are
represented using three size bins. For sea salt, the dry particle diameter ranges are 0.03–0.5, 0.5–5, and 5–20 μm; for dust, the
ranges are 0.03–0.55, 0.55–9, and 9–20 μm.

280

For each of the tracers used in the scheme of Morcrette et al. (2009), wavelength dependent MACs are specified, which are defined
as the extinction cross section per unit dry mass. Thus, the LW absorption is calculated by mapping the modal dry component
masses simulated by TM5 onto these tracers. For sea salt and dust, all of the mass contained in the accumulation modes is put into
the first bin; of the mass in the coarse modes, 22.2 % is put into the second bin and the rest into the third bin. This percentage is
285 based on the assumption that the third bin contains roughly 3.5 times more mass than the second (Morcrette et al., 2009). The
aerosol water simulated by TM5 is not used in this calculation. Instead, water uptake by sulfate, hydrophilic organic aerosols, and
sea salt is taken into account via a dependence of their MACs on relative humidity. For BC, the humidity independent MAC for
the hydrophobic component is applied to both the soluble and insoluble modes. The contributions of ammonium nitrate and MSA
to the LW absorption are neglected.

290

Aerosol activation, i.e. the formation of cloud droplets by heterogeneous nucleation on aerosols, is described following the
activation scheme from Abdul-Razzak and Ghan (2000), which was specifically developed for modal aerosol schemes like M7. It
makes use of Köhler theory to calculate the critical supersaturation and critical particle diameter for each of the relevant water-
soluble modes, assuming uniform internal mixing inside the modes. The hygroscopicity parameters adopted in the model for the
various aerosol components are given in Table 1. The scheme utilizes an approximate expression to calculate the maximum
295 supersaturation for an air parcel rising adiabatically at a constant vertical velocity. This allows to estimate the diameter of the
smallest activated particle per mode and consequently the number of activated particles, as a function of updraft velocity. The
cloud droplet number concentration (CDNC) follows as the total in-cloud number concentration of activated aerosols, which is
determined by averaging over an appropriate probability distribution of updraft velocities. In EC-Earth3-AerChem and other EC-
300 Earth3 configurations, subgrid-scale vertical velocities are described by a Gaussian distribution with mean equal to the large-scale
vertical velocity (see e.g. Morales and Nenes, 2010). The standard deviation of the distribution is set to 0.8 m s⁻¹. The activation is
determined as an average over the range of positive velocities. Currently, this range is sampled using 10 evenly distributed values,
varying from 0.2 to 3.8 times the standard deviation. A minimum CDNC value of 30 cm⁻³ is assumed.

305

For radiation calculations, the effective radius of cloud droplets is determined from the cloud liquid water content provided by the
prognostic cloud scheme and the cloud droplet number concentration (CDNC) from the diagnostic cloud activation scheme,
following Martin et al. (1994) with the drizzle correction from Wood (2000). The resulting droplet effective radius depends on the
simulated aerosol number and mass concentrations, which is an expression of the first aerosol indirect or cloud albedo effect
(Twomey, 1977). To prevent unrealistic values, the effective radius is clipped to 4–30 μm.

310

Autoconversion of cloud droplets into rain is treated using a formulation based on Sundqvist (1978). The rate of precipitation
formation by autoconversion in stratiform clouds is calculated as

$$S = c_0 \times q \times \left(1 - \exp \left[- \left(\frac{q}{qc} \right)^2 \right] \right), \quad (1)$$



where c_0^{-1} is a characteristic time scale, q the cloud liquid water content, and q_c a critical cloud liquid water content at which the autoconversion starts to be efficient. The calculation of q_c and c_0 in EC-Earth3-AerChem and other EC-Earth3 configurations differs from that in IFS cycle 36r4. Instead of using fixed values of q_c over land and ocean as in the original IFS model, a critical volume-mean cloud droplet radius is specified (see e.g. Rotstajn and Penner, 2001). As a result, q_c is directly proportional to CDNC. The value of the critical droplet radius was determined during the tuning of EC-Earth3 and is set to 8.75 μm (see Sect. 3). An additional, weaker dependence on CDNC is introduced via the rate coefficient c_0 (see Wyser et al., 2020). In accordance with other studies (e.g. Rotstajn and Penner, 2001), c_0 is assumed to vary as $N_d^{-1/3}$, where N_d denotes CDNC. With these modifications, the precipitation formation rate in stratiform clouds is made dependent on the simulated aerosol number and mass concentrations, in such a way that the precipitation formation efficiency, S/q , is reduced at larger CDNC. This is an expression of the second aerosol indirect or cloud lifetime effect (Albrecht, 1989).

2.3 Atmospheric chemistry and boundary conditions for chemical tracers

EC-Earth3-AerChem simulates the microphysical and chemical interaction of aerosols and trace gases in the troposphere. The chemistry scheme of TM5 accounts for gas-phase, aqueous-phase and heterogeneous chemistry (van Noije et al., 2014). The gas-phase reaction scheme is a modified version of the CB05 carbon bond mechanism (Yarwood et al., 2005). A first version of the modified scheme (mCB05) was presented by Williams et al. (2013). The scheme employed in EC-Earth3-AerChem is the extended and updated version described by Williams et al. (2017). Photolysis rates are calculated using the modified band approach from Williams et al. (2006; 2012; 2017).

When calculating photolysis rates, scattering and absorption by aerosols are accounted for based on the online simulated optical properties from within TM5 (see Sect. 2.2), without making use of the stratospheric aerosol forcing data set from CMIP6. As a consequence, the radiative effects of large volcanic eruptions are not explicitly accounted for in the photochemistry of the model. Effects of cloud liquid water and ice particles on photolysis rates are included as described by Williams et al. (2012), but with cloud droplet effective radii calculated following the parameterization of Martin et al. (1994), using fixed values of CDNC over land and ocean (313.2 and 42.0 cm^{-3} , respectively, corresponding to aerosol concentrations of 900 and 40 cm^{-3} for particles in the size range 0.1–3 μm diameter), with lower and upper limits set to 4 and 16 μm .

Heterogeneous chemistry is limited to the reactive uptake of dinitrogen pentoxide (N_2O_5) at the surface of cloud droplets, ice particles and aerosols, and the uptake of the hydroperoxyl (HO_2) and nitrate (NO_3) radicals on aerosols. In these reactions one molecule of N_2O_5 produces two molecules of nitric acid (HNO_3), one molecule of NO_3 produces one molecule of HNO_3 , and two molecules of HO_2 produce one molecule of H_2O_2 . These reactions are described using a first-order rate coefficient, which for a mono-disperse distribution of spherical particles of radius r is given by

$$dk(r) = \left(\frac{r}{D_g} + \frac{4}{v\gamma} \right)^{-1} dS(r), \quad (2)$$

where D_g is the gas-phase molecular diffusion coefficient of the reacting species in air, v the mean molecular speed of the species in the gas phase, γ the probability that a molecule impacting the surface undergoes reaction, and $dS(r)$ the surface area density of the particles per unit volume of air (see e.g. Jacob, 2000). The first term between the parentheses on the right-hand side of the equation describes the uptake associated with diffusion to the particle surface, the second term describes the uptake associated with free molecular motion to the particle surface.



Following Huijnen et al. (2014), the uptake of N_2O_5 by heterogeneous reactions in clouds is determined from Eq. (2) by replacing the variable r in the diffusion term by the effective radius r_e of the droplets or ice particles, respectively. Thus, the total rate coefficient is expressed as

$$k = \left(\frac{r_e}{D_g} + \frac{4}{v\gamma} \right)^{-1} S, \quad (3)$$

where S is the total surface area density of the liquid or ice contained in the cloud. The effective radii and surface area densities are calculated as in Williams et al. (2017). In Eq. (3) a temperature dependent reaction probability $\gamma(T)$ is used for the uptake of N_2O_5 on liquid water (Ammann et al., 2013), while a fixed γ value of 0.02 is adopted for the uptake on ice particles (Crowley et al., 2010).

For aerosols the uptake tends to be limited by free molecular motion (Jacob, 2000). When performing the integration of Eq. (2) over particle size and composition, we therefore replace $\left(\frac{r}{D_g} + \frac{4}{v\gamma} \right)$ for all particles in mode i by $\left(\frac{r_{g,i}}{D_g} + \frac{4}{v\gamma_i} \right)$, where $r_{g,i}$ is the geometric mean (i.e. median) radius of the mode and γ_i the reaction probability for that mode. The total rate coefficient is thus given by

$$k = \sum_i \left(\frac{r_{g,i}}{D_g} + \frac{4}{v\gamma_i} \right)^{-1} S_i, \quad (4)$$

where S_i is the total surface area density of the particles contained in mode i . For simplicity, the uptake on aerosols is described using constant values of the reaction probability, irrespective of mode or composition. For N_2O_5 a value of 0.02 is assumed, which corresponds to the global mean value from Evans and Jacob (2005); the reaction probabilities for HO_2 and NO_3 are set to 0.06 and 0.001, respectively, based on Abbatt et al. (2012) and Jacob (2000).

The model includes aqueous-phase reactions for the oxidation of total dissolved sulfur dioxide by dissolved hydrogen peroxide (H_2O_2) and ozone, depending on the acidity of the droplets (van Noije et al., 2014). The acidity calculation is done with a spatially homogeneous CO_2 mixing ratio, which is set equal to the annual and global mean surface value provided in the CMIP6 historical or scenario data sets (Meinshausen et al., 2017; 2020).

Other boundary conditions are applied to constrain the mixing ratios of ozone, carbon monoxide, nitric acid and methane in the stratosphere and that of methane in the lower part of the troposphere (Williams et al., 2017). These boundary conditions are applied through Newtonian relaxation (nudging) towards daily-varying zonal mean fields, obtained from monthly input data sets by linear interpolation in time. Compared to the description given by Williams et al. (2017), the boundary conditions applied for ozone and methane have been modified for CMIP6, as described below.

The mixing ratios of ozone in the stratosphere are nudged towards zonal mean fields calculated from the three-dimensional input data sets provided by CMIP6 (Checa-Garcia et al., 2018). For ozone, these consist of a climatology for the pre-industrial period and transient data sets for the historical period and the four tier-1 scenarios from ScenarioMIP (O'Neill et al., 2016). The zonal means from the input files are mapped onto the TM5 grid, using a local mass conserving regridding scheme in the vertical direction (and linear interpolation in the meridional direction).

The evolution of methane is constrained by the surface mixing ratio data provided by CMIP6 (Meinshausen et al., 2017; 2020). In the lower troposphere, the mixing ratios of methane are nudged towards zonal mean values calculated from the CMIP6 input data,



using a relaxation time constant of 2.5×10^5 s or 2.9 days (Bándá et al., 2014). The domain where this nudging is applied extends from the surface to the highest model layer with full-level pressure above 550 hPa for a surface pressure of 984 hPa. Area averaging is applied to coarsen the zonal mean input fields from a meridional resolution of 0.5° to 2° in TM5. In the stratosphere, methane is nudged to a climatology derived from measurements made by the HALOE (Halogen Occultation Experiment) satellite instrument (Groß and Russell, 2005) scaled according to the time series of the annual and global mean surface mixing ratio provided by CMIP6. Following the recommendation of Meinshausen et al. (2017), we assume there is a delay of one year between mixing ratios at the surface and in the stratosphere. Because the HALOE measurements were made from October 1991 to August 2002, we assume that the climatology is representative of the 10-year period 1992–2001, which translates to 1991–2000 at the surface. Thus, the scale factor is defined as the ratio of the global mean mixing ratio in a particular year and the average over 1991–2000.

400

The ozone and methane mixing ratios from TM5 are input to the SW and LW radiation schemes of IFS. The methane mixing ratios are also used in IFS to determine the production of water vapour by oxidation of methane in the stratosphere. This calculation makes use of the same parameterization as in EC-Earth3 (see Döscher et al., in preparation).

405 **2.4 Anthropogenic and natural emissions**

This section gives an overview of the emissions of reactive gases and aerosols applied in TM5. The amounts of emissions from anthropogenic activities and open biomass burning are specified using data sets provided by CMIP6 (Feng et al., 2020): historical anthropogenic emissions are taken from the Community Emissions Data System (CEDS; Hoesly et al., 2018), historical fire emissions from the BB4CMIP6 data set (van Marle et al., 2017), and future emissions from the respective scenario data sets (Gidden et al., 2019). Anthropogenic and biomass burning emissions for the historical period are provided as monthly and annually varying fields. An exception is the anthropogenic emissions of methane prior to 1970, for which monthly emissions are only provided at 10-year intervals. Scenario emissions are provided for 2015 and from 2020 onwards also at 10-year intervals. For these cases, the emissions in intermediate years are calculated by linear interpolation.

415 Biogenic emissions of non-methane volatile organic compounds (NMVOCs) and carbon monoxide (CO) are prescribed using monthly estimates from the MEGAN-MACC data set (Sindelarova et al., 2014) for the year 2000. Distinct diurnal cycles are applied to the biogenic emissions of isoprene and monoterpenes (Bergman et al., in preparation). Speciated anthropogenic NMVOC emissions are provided for all sources, except for the aircraft sector. Following the recommendations from the CEDS team, the NMVOC emissions from the aircraft sector are split using distinct NMVOC profiles for the contributions from in-flight exhaust and takeoff and landing. Natural methane emissions and the rate coefficients describing the uptake of methane by soils are prescribed using estimates from Spahni et al. (2000) for the year 2000. The sources of mineral dust and sea salt, the oceanic source of DMS, and the production of nitrogen oxides (NO_x) by lightning are calculated online, as described below. All other natural emissions are prescribed as documented in van Noije et al. (2014). These include terrestrial DMS emissions from soils and vegetation, biogenic emissions of NO_x and ammonia (NH_3) from soils, oceanic emissions of CO, NMVOCs and NH_3 , and SO_2 fluxes from continuously emitting volcanoes.

425

The dust source is calculated using the scheme developed by Tegen et al. (2002). It is based on the assumption that a particle can be released from the soil when the surface friction velocity exceeds a certain threshold value, which depends on the size of the particle and the roughness of the surface (Marticorena and Bergametti, 1995). The threshold friction velocity is determined using a monthly climatology of roughness lengths derived from scatterometer observations from the European Remote Sensing (ERS)

430



satellite (Prigent et al., 2005; see also Cheng et al., 2008). In grid cells with a substantial fraction of cultivated land, the dust source is enhanced by reducing the threshold friction velocity by up to 27 %, following a similar approach as in Tegen et al. (2004). Currently, the fractional cropland areas assumed in this calculation are based on a data set for 1992 (Ramankutty and Foley, 1999). The vertical flux of dust particles is subsequently calculated as a function of particle size and the 10 m horizontal wind speed following Tegen et al. (2002). The grassland and shrubland area fractions that enter this calculation are determined from the vegetation fields received from IFS. Snow covered areas are excluded as dust sources; the snow cover is estimated from the snow depth as in Tegen et al. (2002). Soil moisture effects are presently not accounted for.

The vertical flux is calculated for four size bins with radius boundaries at 0.1, 0.3, 0.9, 2.7, and 8.0 μm (actually 8.0 divided by 3^n with integer number n running from 4 to 0). The resulting size-resolved flux is subsequently mapped to the accumulation and coarse modes of M7 with mass median radius set to 0.37 and 1.75 μm and geometric standard deviation of 1.59 and 2.0, respectively (Stier et al., 2005). The weights of the distributions are determined such that the respective mass fluxes in the intervals covered by the first bin and by the second to fourth bins are exactly conserved. The mass and number fluxes associated with these two lognormal distributions are put into the insoluble accumulation and coarse modes, respectively. The global dust emission is tuned by applying a constant correction factor to the threshold friction velocity (Tegen et al., 2004; Cheng et al., 2008). This factor has been set to 0.6 (see Sect. 3).

The source of sea salt is calculated following Gong et al. (2003) with a temperature dependence based on Salter et al. (2015). The flux of the number of sea-spray particles formed over ice-free ocean areas is expressed as a function of the particle radius at 80 % humidity and the 10 m horizontal wind speed, U_{10} , using the parameterization from Gong et al. (2003). In this formulation the ocean whitecap coverage fraction, W , is related to U_{10} as $W = 3.84 \times 10^{-6} \times U_{10}^{3.41}$ (Monahan and Muircheartaigh, 1980). This size-resolved flux is approximated by two lognormal distributions with number median dry radius of 0.09 and 0.794 μm and geometric standard deviation of the accumulation and coarse modes of M7, respectively (Vignati et al., 2010a). The weights of the distributions are determined by requiring that the mapping conserves the integrated number fluxes of particles with dry radius in the ranges 0.05–0.5 and 0.5–5 μm . It is assumed that the emitted sea-spray particles consist of sea salt only. The particle number and sea-salt mass fluxes associated with these two lognormal distributions are put into the soluble accumulation and coarse mode, respectively.

Several studies have indicated that the formation of sea spray depends on the sea water temperature and that this temperature dependence changes the size distribution of the formed particles (e.g. Mårtensson et al., 2003; Ovadnevaite et al., 2014; Salter et al., 2014). Following the approach of Salter et al. (2015), we describe the temperature effect using distinct multiplication factors for the particle fluxes in the accumulation mode, f_a , and coarse mode, f_c . These factors are given by:

$$f_a(T) = -8.75593 \times 10^{-5} \times T^3 + 5.56771 \times 10^{-3} \times T^2 - 0.11670 \times T + 1.79321 \quad \text{for } -1 \leq T \leq 15 \text{ }^\circ\text{C} \quad (5)$$

$$f_c(T) = 3.75294 \times 10^{-2} \times T + 0.43706 \quad \text{for } -1 \leq T \leq 30 \text{ }^\circ\text{C}, \quad (6)$$

where T is the sea surface temperature (SST) in degrees Celsius and coefficients have been rounded to five decimals. No temperature dependence is assumed outside the indicated ranges. Equations (5) and (6) are simplified forms of the empirically derived polynomial expressions from Salter et al. (2015) for their modes with number median radii of 0.0475 and 0.75 μm , respectively, which have been scaled to 1.0 at a reference SST value of 15 $^\circ\text{C}$. Figure 1 shows the temperature factors f_a and f_c as functions of the SST.

470



The DMS flux in ice-free ocean areas can be calculated as the product of the local surface ocean DMS concentration and the gas transfer velocity (e.g. Lana et al., 2011). The ocean concentrations are prescribed according to the monthly climatology from Lana et al. (2011). The gas transfer velocity is parameterized following Wanninkhof (2014). It is proportional to U_{10}^2 and depends on the SST through the Schmidt number. The Schmidt number is expressed as a fourth-order polynomial of the SST.

475

The amount of NO_x produced in lightning discharges is calculated using an improved version of the parameterization described by Huijnen et al. (2010). Compared to earlier model versions (e.g. Huijnen et al., 2010; van Noije et al., 2014), the distribution between cloud-to-ground (CG) and intra-cloud (IC) discharges has been corrected for clouds for which the thickness of the cold sector is less than 5.5 km. Previously, the percentage of CG discharges was set to 0 % for these clouds; this has now been changed to 100 % (Price and Rind, 1994). As a second revision, it is now assumed that IC flashes are as efficient in producing NO_x as CG flashes (Ridley et al., 2005; Ott et al., 2010). The amount of NO_x produced by each flash is still scaled by a constant factor to ensure that the global total production is around 6 Tg N yr⁻¹ (see Sect. 3).

480

As in earlier versions of the model the emissions of black carbon, primary organic aerosols and sulfate are characterized using lognormal size distributions with the same geometric standard deviation as the corresponding modes in M7. Previously, carbonaceous aerosols were emitted in the Aitken modes of M7 using size distributions with a number median radius of 0.040 μm for open biomass burning and 0.015 μm for all other sources (aan de Brugh et al., 2011). These values were taken from Dentener et al. (2006), without correcting for the fact that the Aitken modes in M7 have a different geometric standard deviation than the distributions recommended in that study. All of the BC emissions were put into the insoluble mode, while 65 % of the emitted POA mass was assumed to be water soluble irrespective of the source of the emissions (Stier et al., 2005). In the current model version, the carbonaceous emissions are described using an Aitken-mode distribution for the insoluble particles and an accumulation-mode distribution for the soluble particles (see Table 4). Following Stier et al. (2005), the number median radii of these distributions are set to 0.030 and 0.075 μm , respectively. Carbonaceous emissions from solid biofuel burning and open biomass burning are now assumed to have similar characteristics: for both POA and BC it is assumed that 95 % of the mass from these sources is emitted in the (soluble) accumulation mode (see Sect. 3). BC and POA emissions from other sources are assumed to be insoluble.

485

490

495

Table 4. Distribution of the carbonaceous aerosol emissions from open biomass burning, biofuel burning and other sources over the insoluble Aitken and soluble accumulation modes, as mass percentages.

	Insoluble Aitken	Soluble accumulation
Black carbon (BC)		
Open biomass burning	5.	95.
Biofuel burning	5.	95.
Other sources	100.	0.
Primary organic aerosols (POA)		
Open biomass burning	5.	95.
Biofuel burning	5.	95.



Other sources	100.	0.
---------------	------	----

500

Following the recommendation by Dentener et al. (2006), 2.5 % of the emitted SO_x mass is assumed to be emitted in the form of SO₄ particles. These particulate emissions are distributed over the soluble Aitken, accumulation and coarse modes, using three lognormal size distributions with number median radii set to 0.030, 0.075 and 0.75 μm, respectively (Stier et al., 2005). The distribution of the emitted SO₄ mass from the various sources and sectors over the three modes has been revised as indicated in Table 5. Previously, 100 % of the emissions from the industrial sector were put into the accumulation mode, and 50 % of the emissions from all other sources and sectors were put into the Aitken mode and the other 50 % in the accumulation mode (aan de Brugh et al., 2011). The new distribution more closely follows the recommendations from Dentener et al. (2006).

505

510 Table 5. Distribution of the sulfate emissions from the various sources and sectors over the soluble Aitken, accumulation and coarse modes, as mass percentages.

	Aitken	Accumulation	Coarse
Industrial sector	0.	50.	50.
Energy sector	0.	50.	50.
International shipping	0.	50.	50.
Open biomass burning	0.	100.	0.
Volcanoes (non-explosive)	50.	50.	0.
Other sources and sectors	100.	0.	0.

All emissions except those from the aircraft sector are provided as two-dimensional fields and are distributed over model layers using the vertical profiles given in Table A1 of van Noije et al. (2014). Here the emissions from open biomass burning, including those from grassland fires and agricultural waste burning, are distributed according to the profiles defined for forest fires.

515

2.5 Technical and numerical aspects

The atmospheric grid of TM5 is a regular latitude-longitude grid with a resolution of 3° × 2° (longitude × latitude). The base time step of the model is 1 h, but the time step is dynamically reduced where needed to fulfil the Courant-Friedrichs-Lewy (CFL) stability criterion (Krol et al., 2005; Huijnen et al., 2010). To avoid the need for very short time steps, a reduced grid is applied in the zonal advection routine. In the reduced grid, the number of grid points in the zonal direction gradually decreases when approaching the poles. By merging cells, the number per latitude band is reduced from 120 equatorward of 76° to 40 between 76 and 78°, 8 between 78 and 82°, 4 between 82 and 88°, and 2 between 88 and 90°. The TM5 grid consists of 34 hybrid sigma-pressure layers in the vertical direction, which have been constructed by merging of layers defined on the IFS grid. Except for the top layer, all layers in TM5 are combinations of two or three adjacent layers in IFS. The top layer corresponds to five layers in IFS and has a full-level pressure of ~ 0.1 hPa.

520

525



530 Details about the OASIS data exchange between IFS and TM5 are given in van Noije et al. (2014). Their Table 1 gives a list of
the atmospheric and surface fields transferred from IFS to TM5. Grid point atmospheric fields are interpolated from the N128
reduced Gaussian grid to the TM5 $3^\circ \times 2^\circ$ grid. To make use of the higher resolution in IFS, surface fields are interpolated to $1^\circ \times$
 1° and applied at this resolution in TM5 to calculate dry deposition velocities and the sources of mineral dust, sea salt and oceanic
DMS. The west-east and south-north components of the 10 m wind are not used by TM5 anymore and have been replaced by the
10 m wind speed; furthermore, the sea surface temperature, needed in the calculation of the production of sea spray and the oceanic
535 DMS flux, has been added as an instantaneous field.

Table 6 lists the fields IFS receives from TM5, and where they are applied. These fields are all three-dimensional and instantaneous.
Mass mixing ratios are passed for all M7 components (including OA, but not POA and SOA separately) as well as nitrate and
MSA. Since nucleation-mode particles can be neglected for cloud activation and LW radiative effects, the associated number and
mass mixing ratios are not included in the data transfer. The aerosol optical properties fields are the extinction, single-scattering
540 albedo and asymmetry factor at the 14 wavelength bands of the RRTMG SW radiation scheme (see Sect. 2.2). We recall that the
model distinguishes between stratospheric and tropospheric aerosols, and that the TM5 aerosol fields are only used by IFS in the
troposphere. The transfer of aerosol fields and the calculation of the optical fields for RRTMG_{sw} are therefore limited to the lowest
23 layers, i.e. the domain extending from the surface to 73.4 hPa. The convection calculations in TM5 are limited to the same
545 domain.

Table 6. Fields transferred from TM5 to IFS.

Field	Application in IFS	Domain of application
Methane mixing ratio	SW and LW radiation scheme	Whole atmosphere
Ozone mixing ratio	SW and LW radiation scheme	Whole atmosphere
Aerosol number mixing ratio per mode	Cloud activation scheme	Troposphere
Aerosol component mass mixing ratios per mode	Cloud activation scheme, LW radiation scheme	Troposphere
Aerosol optical properties	SW radiation scheme	Troposphere

550 The time interval of the data exchange between IFS and TM5 is 6 h. This is eight times the time step in IFS and six times the base
time step in TM5. To put this into perspective, note that during many years the standalone configuration of TM5 has been driven
by 6-hourly meteorological fields and that the full radiation computations in IFS (cycle 36r4) are done only every 3 h (Morcrette
et al., 2000). It would be possible to increase the exchange frequency to 3 h, but this would lead to a substantial decline of the
computational performance.

555 Built around the OASIS3-MCT coupler, the synchronization of IFS and TM5 has been overhauled. On the IFS side, it uses the
new coupling interface introduced in EC-Earth3 (Döscher et al., in preparation). The two models still run concurrently but TM5
execution is not delayed by a full coupling interval anymore. Indeed, in the previous implementation, TM5 could start simulating
the next 6-hourly interval only once IFS had reached the end of it (van Noije et al., 2014). The advantage was that TM5 knew the
pressure at the beginning and end of the coupling interval without any lag, and could adjust the horizontal air mass fluxes to close



560 the air mass balance and ensure mass conservative transport of tracers during that interval (Segers et al., 2002). The new approach
 removes the 6 h delay, making the execution of TM5 and IFS more synchronous, but introduces a lag (as defined by OASIS3-
 MCT) of 45 min for the fields received by TM5 (i.e. one IFS time step). Although only the fields at the beginning of the interval
 are known now, TM5 still applies a mass conservative transport operator. This leads to a surface pressure that slightly diverges
 from its IFS counterpart but is correctly reset at the start of the next coupling interval. The new design has some important
 565 advantages. It removes the need to run the models sequentially when the feedback from TM5 to IFS is switched on. Moreover, that
 feedback occurs with a lag of 1 h (one TM5 timestep) instead of 3 h (half a coupling interval) previously. Equally as important, it
 greatly facilitates coupling additional components to TM5, like a dynamic global vegetation model and/or an ocean
 biogeochemistry component. This capability was exploited to develop a carbon-cycle configuration of EC-Earth3 (Döscher et al.,
 in preparation).

570 The large amount of data exchanged with TM5 has always been hindering the model performance. Several steps have been taken
 to alleviate this issue (see Table 7). First, since TM5 runs on a subset of IFS levels, the reduction operation was moved from TM5
 to IFS to decrease the amount of multi-level data transferred to TM5, which halved the execution time. An additional 40 %
 performance increase was obtained by packing several levels together into one OASIS3-MCT entry, taking advantage of the new
 575 bundle feature of the coupler (Craig et al., 2017). Finally, the parallelization of TM5 with the Message Passing Interface (MPI)
 library has been revised. The domain decomposition now consists in a geographical partitioning (Williams et al., 2017). This has
 strongly improved the scalability of the TM5 model, and also enabled all MPI tasks to communicate with OASIS3-MCT,
 essentially parallelizing the exchange of grid-point fields. In the model version described by van Noije et al. (2014), only one TM5
 core was communicating with OASIS3. Although the transfer of spectral fields cannot be distributed in the same fashion, the multi-
 580 core coupling of grid-point fields has improved the performance by 35 %. The last improvement stems from limiting the transfer
 of aerosol fields to 23 out of 34 levels, which corresponds to the domain where convection is applied in TM5 with a top at about
 70 hPa.

585 Table 7. Computational speed in simulated years per day (SYPD) for different implementations of the data exchange between TM5
 and IFS. The benchmark tests were primarily conducted on the high-performance computer of the ECMWF. Performances from
 additional platforms with the final CMIP6 configuration are also reported.

Iteration	Computational speed (SYPD)	Platform
Transfer IFS fields on 91 vertical levels	~ 0.4	Cray XC30 (ECMWF)
Transfer IFS fields on 34 vertical levels	~ 0.87	Cray XC30 (ECMWF)
Transfer IFS fields on 34 vertical levels in three bundles	~ 1.4	Cray XC30, XC40 (ECMWF)
Switch to multi-core coupling (grid-point IFS and TM5 fields)	~ 2.0	Cray XC40 (ECMWF)
Transfer TM5 aerosol fields on 23 out of 34 levels	2.3–3.2	Cray XC40 (ECMWF, SMHI, CSC), Atos Bullx B500 (KNMI), ClusterVision Tetralith (NSC)



In its latest iteration with load balancing and optimization of bundle sizes, EC-Earth3-AerChem runs at about 3 simulated years per day (SYPD; Balaji et al., 2017) on the most recent platforms. This can be compared to the standard EC-Earth3 model and its high-resolution configuration, which typically reach 15–20 and 2–4 SYPD (Haarsma et al., 2020), respectively. Clearly, performance-wise, the increased complexity from interactive aerosols and atmospheric chemistry costs about as much as increasing the horizontal resolution of the model (by a factor of 2 and 4 for the atmosphere and ocean components, respectively).

3 Tuning and spin-up

As a first step in the tuning process, a small number of parameters in TM5 were optimized in a standalone configuration driven by meteorological and surface fields from the ERA-Interim reanalysis (Dee et al., 2011) using the same horizontal resolution and number of vertical levels as in EC-Earth3-AerChem (see van Noije et al., 2014). Specifically, the correction factor for the threshold friction velocity applied in the calculation of the mineral dust source was set to 0.6, resulting in a global source of 1.12×10^3 Tg in the year 2010. This is well within the range obtained in other global models (e.g. Huneceus et al., 2011; Gliß et al., 2020), although for a proper comparison of emitted mass amounts from different models one should account for differences in the representation of the upper end of the size distribution. Moreover, the scale factor applied to the NO_x produced in lightning flashes was determined from the requirement that the total production in 2006 is 6.0 Tg N.

The assumptions about the size distribution and solubility of carbonaceous aerosols emitted from biofuel and open biomass burning have also been revised as part of the tuning. Initially, 65 % of the organic matter from open biomass burning was assumed to be water soluble, consistent with observations (Mayol-Bracero et al., 2002; Reid et al., 2005). POA emissions from other sources, including solid biofuel burning, as well as freshly emitted BC were assumed to be 100 % insoluble and thus emitted in the Aitken mode. This resulted in too high particle number concentrations in residential regions with substantial biofuel burning. The carbonaceous emissions from solid biofuel burning have therefore been separated from the other emissions in the residential sector and are treated as emissions from open biomass burning. In an intermediate version of the model, 50 % of the BC mass emitted by biofuel and biomass burning was assumed to be emitted into the (soluble) accumulation mode (see e.g. Kodros et al., 2015). In line with measurements of the size distributions of emissions from open biomass burning (Janhäll et al., 2010) and biofuel burning (Li et al., 2009; Winijkul et al., 2015), this percentage has later been increased to 95 % for both POA and BC. This revision has led to modest reductions in the aerosol optical depth in parts of East Asia and, during boreal winter and spring, in Western Africa and the tropical Atlantic, improving the comparison with observations in these regions (not shown). An evaluation of aerosol optical properties for the year 2010 simulated with the final parameter settings in TM5 is presented by Gliß et al. (2020). This evaluation includes both the TM5 standalone configuration driven by meteorological and surface fields from the ERA-Interim reanalysis (Dee et al., 2011) and the EC-Earth3-AerChem model in atmosphere-only configuration with sea surface temperatures (SSTs) and sea ice concentrations prescribed as in the Atmospheric Model Intercomparison Project (AMIP) experiment (Döscher et al., in preparation) and atmospheric temperatures and surface pressures nudged to ERA-Interim fields.

The tuning of the model's climate started from the tuned configuration of EC-Earth3 (Döscher et al., in preparation). As explained in the introduction, the main differences between the two configurations are due to tropospheric aerosols and tropospheric and lower-stratospheric ozone. In EC-Earth3, tropospheric aerosols are described by the MACv2-SP simple plume representation of anthropogenic aerosol optical properties and cloud effects (Stevens et al., 2017) in combination with a pre-industrial climatology produced by TM5.



EC-Earth3 produces an aerosol effective radiative forcing (ERF) of about -0.8 W m^{-2} over the CMIP6 historical period (1850–2014), as estimated from a set of 30-year atmosphere-only simulations performed as part of the Radiative Forcing Model Intercomparison Project (RFMIP; Pincus et al., 2016). For comparison, using the same IFS parameter settings as in EC-Earth3, the aerosol ERF in EC-Earth3-AerChem was estimated at -1.1 W m^{-2} . The final revision of the treatment of carbonaceous emissions from biofuel and biomass burning emissions resulted in a $\sim 0.4 \text{ W m}^{-2}$ weaker aerosol forcing, bringing the forcing in EC-Earth3-AerChem closer to that in EC-Earth3. This is mainly due to a reduction in the SW cloud forcings, as we have verified using the method proposed by Ghan (2013). (The aerosol ERF estimates for both configurations were obtained from 15-year simulations with AMIP SSTs and sea ice concentrations for the years 2000–2014, as the difference in the net energy imbalance at the top of the atmosphere (TOA) between simulations with emissions for 2000–2014 and 1850, respectively. To isolate the effects of tropospheric aerosols, the mixing ratios of methane and ozone in these simulations were prescribed in IFS as in EC-Earth3.)

In view of these results, our tuning efforts focused on the pre-industrial climate of EC-Earth3-AerChem; no attempt was made to make specific adjustments to improve the model’s climate for the present day or the simulated warming over the historical period. When tuning the pre-industrial climate of EC-Earth3-AerChem, a small number of atmospheric tuning parameters in IFS has been re-adjusted, leaving ocean and sea ice parameters in NEMO untouched. The model was initialized from the IFS and NEMO states taken from the EC-Earth3 pre-industrial control simulation (member r1i1p1f1, after 500 years), and a TM5 state representative of pre-industrial conditions. (After 10 years, a small update of the pre-industrial vegetation climatology was introduced. This had only a minor impact on the simulated pre-industrial climate.) Without re-adjusting any tuning parameters in IFS the model started to drift to a new climate state, characterized by higher temperatures especially in the Northern Hemisphere. The increase in zonal mean surface air temperatures varied from less than a few tenths of a degree in the mid-latitudes of the Southern Hemisphere to a few degrees at high latitudes in the Northern Hemisphere, turning the cold biases of EC-Earth3 into warm biases in these regions. Informed by a comparison with the ERA5 reanalysis for the 1980s (Herschbach et al., 2020), corrected for the observed warming since pre-industrial times, we tried to reduce these warm biases by re-adjusting a small set of tuning parameters in IFS. Based on experience gained during the tuning of EC-Earth3 (Döscher et al., in preparation), three parameters were selected affecting both warm and cold regions: ENTRORG, the fractional entrainment (m^{-1}) for positively buoyant deep convection divided by the gravitational constant; RSNOWLIN2, which governs the temperature dependence of the autoconversion of ice crystals to snow in large-scale precipitation (Lin et al., 1983); and RLCRIT_UPHYS, the critical cloud droplet radius for the autoconversion of droplets into rain in large-scale precipitation (see Sect. 2.2). Using parameter sensitivities derived from EC-Earth3 atmosphere-only simulations, two combinations of settings were defined corresponding to a target global mean surface cooling of 0.5 and 0.75 °C (see Table 8).

Table 8. Parameter settings for the three IFS parameters that have been re-adjusted for tuning the model’s pre-industrial climate. The column labelled ‘EC-Earth3-AerChem’ contains the values adopted in the CMIP6 configuration of the model, which correspond to a target reduction in the global mean surface temperature of 0.5 °C compared to the configuration with the standard EC-Earth3 settings. The settings indicated in the column labelled ‘EC-Earth3-AerChem, cold variant’ correspond to a target surface cooling of 0.75 °C.

Tuning parameter	IFS cycle 36r4	EC-Earth3	EC-Earth3-AerChem	EC-Earth3-AerChem, cold variant
ENTRORG ($\text{s}^2 \text{ m}^{-2}$)	1.8×10^{-4}	1.7×10^{-4}	1.75×10^{-4}	1.75×10^{-4}



RSNOWLIN2 (K ⁻¹)	0.025	0.035	0.030	0.029
RLCRIT_UPHYS (m)	Not applied	8.75×10^{-6}	8.75×10^{-6}	8.84×10^{-6}

665 Initially, the focus was on the cold variant of the model. A sensitivity simulation for this configuration was started by branching
off from the reference simulation with standard EC-Earth3 settings (after about 20 years from the start). As expected, the
configuration with adjusted settings produced a colder climate. The Northern Hemisphere was more strongly affected than the
Southern Hemisphere: at northern high latitudes, the zonal mean surface air temperature was reduced by more than 2 °C. After
another ~ 100 years, a third simulation was started with parameter settings as in the final EC-Earth3-AerChem configuration (see
670 Table 8). This simulation branched off from the reference simulation. After having completed a few decades, the reference
simulation was stopped and the two sensitivity simulations were continued for another ~ 90 years. At that point it was discovered
that the correction factor for the dust source was set to 0.7, a value obtained for an intermediate version of EC-Earth3-AerChem,
resulting in a reduction of the global source to about 550 Tg yr⁻¹ in these simulations. After resetting the factor to the intended
value of 0.6, a new set of simulations was launched for the three configurations indicated in Table 8. This increased the dust source
675 to about 1.1×10^3 Tg yr⁻¹, as verified from the first few years of the simulations. The configuration with a cooling target of 0.5 °C
produced satisfactory behavior for the same set of atmosphere and ocean variables considered in the tuning of EC-Earth3 (Döscher
et al., in preparation), and was spun up for 300 years. Compared to EC-Earth3, this configuration produced higher, more realistic
pre-industrial temperature levels in the Northern Hemisphere, resulting in reduced long-term variability in the global mean surface
temperature. While running the CMIP6 historical simulation with the selected parameter settings, another bug was discovered in
680 the code dealing with the stratospheric aerosols. This bug affected only EC-Earth3-AerChem, and led to spurious warming by
absorption of SW radiation in the stratosphere. This resulted in a completely wrong response to large volcanic eruptions. After
fixing this bug, the pre-industrial spin-up simulation was continued for another 150 years. The impact of the bug fix on pre-
industrial surface climate turned out to be small. This completed the tuning and spin-up of the model, totalling to 770 continuous
years for the final configuration (on top of the EC-Earth3 pre-industrial control simulation).

685 4 Results

In this section we present results from some of the core CMIP6 simulations conducted with EC-Earth3-AerChem. Here we only
include results from simulations with active ocean and sea ice components. An analysis of the AMIP simulation and AerChemMIP
atmosphere-only simulations will be presented elsewhere. The CMIP6 historical simulation is compared against observational
datasets, using all four available realizations (see Sect. 4.3). For other experiments, the EC-Earth3-AerChem results presented in
690 this paper are based on a single realization (r1i1p1f1).

4.1 Pre-industrial control simulation

Figure 2 shows the time series of the annual mean global surface air temperature (GSAT) and net radiative flux at the top of the
atmosphere (TOA) from the pre-industrial control simulation (piControl). Currently, output from 311 years of piControl is
695 available. This is sufficient to serve as a reference for our four-member ensemble of coupled historical and future simulations
covering 1850–2100, where the different realizations have branching times that lie 20 years apart (see Sect. 4.3). The mean GSAT
is 14.05 ± 0.16 °C, where the standard deviation describes the natural interannual variability. The corresponding range for EC-
Earth3 is 13.87 ± 0.22 °C, as determined from ensemble member r1i1p1f1, which covers 501 years. Hence, in agreement with the
goals set during the tuning phase, EC-Earth3-AerChem is slightly warmer and exhibits lower natural variability than EC-Earth3.
700 The linear trend in GSAT is -0.075 ± 0.009 °C per century. Most of this negative trend is caused by the relatively large low-



temperature excursion that shows up near the end of the simulated period. The mean TOA flux is $-0.10 \pm 0.25 \text{ W m}^{-2}$. The drift in the TOA flux is statistically insignificant at the $p=0.05$ level ($2.1 \pm 15.6 \text{ mW m}^{-2}$ per century).

4.2 Climate sensitivity

705 In this section we present estimates of the model's climate sensitivity obtained from the two DECK CO₂ perturbation experiments. Figure 3a shows the time series of the annual mean GSAT change in these simulations relative to the unperturbed, pre-industrial control simulation. Here the pre-industrial reference values are given by a linear fit through the corresponding 150-year section of piControl. By definition, the transient climate response (TCR) is calculated as the mean GSAT change in the experiment with atmospheric CO₂ concentrations increasing by 1 percent per year (1pctCO₂) in a 20-year period centred around the time of CO₂
710 doubling (i.e. simulation years 60–79; e.g. Meehl et al., 2020). This results in a TCR estimate of 2.1 °C, which is slightly lower than the corresponding estimate of 2.3 °C obtained for EC-Earth3 (from 1pctCO₂ member r3i1p1f1) and in the middle of the range produced by CMIP6 models. For instance, Meehl et al. (2020) obtained a multi-model mean TCR of 2.0 °C with a standard deviation of 0.4 °C, based on CMIP6 model data available from the Earth System Grid Federation (ESGF) in March 2020.

715 The model's effective climate sensitivity can be obtained from the experiment with quadrupled CO₂ concentrations (abrupt-4×CO₂) by linearly regressing the annual mean net TOA flux change versus the annual mean GSAT change (Gregory et al., 2004; Andrews et al., 2012; Meehl et al., 2020; Sherwood et al., 2020), where a consistent definition of change is applied to both variables. Hence, the TOA flux change is corrected for the offset and drift in the corresponding section of the control simulation. Note that neither the TOA flux nor the global temperature shows a statistically significant drift in piControl over this 150-year period. The
720 effective sensitivity is determined from the regression line as the GSAT change at the point where the net TOA flux change reaches zero, divided by 2.0 to convert to double CO₂. We have tested both ordinary least squares (OLS) regression and the Theil-Sen regression method, which is more robust to outliers, and applied these regression methods to the full 150-year period, as well as to restricted periods leaving out the first five (Wyser et al., 2020) or 20 years (e.g. Meehl et al., 2020). All methods produce a sensitivity estimate of 3.9 °C. (OLS regression yields 3.86, 3.92 and 3.92 °C for the 150-, 145- and 130-year periods; the
725 corresponding estimates from the Theil-Sen regression method are 3.86, 3.89 and 3.85 °C.) As an example, Fig. 3b shows the linear fit obtained with Theil-Sen regression applied to the full 150-year period. The value of 3.9 °C is close to the CMIP6 multi-model mean of $3.7 \pm 1.1 \text{ °C}$ from Meehl et al. (2020), but at the high end of the likely range estimated from multiple lines of evidence in the recent study by Sherwood et al. (2020). Applying the same regression methods to the EC-Earth3 abrupt-4×CO₂ experiment (members r3i1p1f1 and r8i1p1f1) results in a sensitivity estimate of around 4.3 °C. The lower estimate for EC-Earth3-
730 AerChem is consistent with the reduction in TCR, and in better agreement with the assessment by Sherwood et al. (2020).

4.3 Evaluation of surface air temperatures in the CMIP6 historical simulation

In this subsection we present surface air temperatures (SATs) from the four available realizations of the CMIP6 historical simulation and evaluate the results against observational datasets. The different ensemble members have been initialized from the
735 pre-industrial control simulation, using branching times 20 years apart. The first member (r1i1p1f1) has been started from the initial state of piControl, and the second (r2i1p1f1), third (r3i1p1f1) and fourth member (r4i1p1f1) from the state obtained after 20, 40 and 60 years of piControl, respectively.

Figure 4 shows the evolution of the annual mean GSAT in the four integrations, together with the corresponding ensemble median and mean values and the range bounded by one standard deviation (σ) around the mean. For comparison, the figure also shows the
740



corresponding time series from the first 165 years of the pre-industrial control simulation. The evolution of the global temperature during the 20th century differs strongly among the four members. Apart from short-term cooling events after large volcanic eruptions, the first, second and fourth members remain relatively close to the pre-industrial mean until about 1950. In contrast, the third member is in a significantly colder state during most of the 20th century. In this period, the spread among the four members exceeds the range of internal variability displayed by the pre-industrial simulation. The ensemble median is higher than the mean for most years in the period 1920 to 1960. In the earlier and later periods, the differences between the median and mean are small. The mean GSAT in the final 10 years of the historical simulation (2005–2014) is 14.76 ± 0.19 °C, where the standard deviation indicates the ensemble spread. This is 0.71 °C above the pre-industrial mean.

In Fig. 5 the median, mean and 1- σ range of annual temperature anomalies are compared against the GISS Surface Temperature Analysis (GISTEMP) version 4 (Lenssen et al., 2019; GISTEMP Team, 2020) and version 2.0 of the temperature reconstruction by Cowtan and Way (2014; 2020). Both data sets combine SAT anomalies over land and sea ice with SST anomalies over open sea. Whereas surface air and water temperatures may be very different, their anomalies are very similar over open sea. We can therefore directly compare the SAT anomalies simulated by the model with the reconstructed anomalies. A more robust comparison would use a blend of air and water temperatures also from the model (Cowtan et al., 2015), but such an analysis is beyond the scope of this paper. The anomalies shown in the figure are calculated with respect to the period 1850–1900 or, for GISTEMP, 1880–1900. The simulated mean GSAT in this period is 14.15 ± 0.08 °C, almost 0.1 °C higher than the average over the pre-industrial control simulation.

Figure 5a shows that the ensemble of four realizations tends to underestimate the observed global temperature anomalies from the end of the 19th century onwards. The upper end of the 1- σ range follows the observational time series reasonably well until the middle of the 20th century. In contrast to the observations, the warmer members show a substantial global cooling during the 1950s and 1960s (see Fig. 4), partly caused by the eruption of Mount Agung in 1963. As a result, all members produce negative anomalies from the 1960s to the end of the 1980s, while the observed anomalies remain positive during these years. In the final decades of the historical period, the simulations tend to overestimate the observed warming trend. The mean GSAT anomaly for the years 2005–2014 is 0.62 ± 0.23 °C. For this period, the GISTEMP and Cowtan and Way time series give a global warming of 0.87 and 0.89 °C, respectively. As can be seen in Fig. 5b and c, the spread among ensemble members as well as the discrepancies with the observed time series are almost entirely caused by variability in Northern Hemisphere (NH) temperatures. The simulated temperature anomalies for the Southern Hemisphere (SH) agree rather well with the GISTEMP time series. The ensemble mean for the period 2005–2014 is 0.69 ± 0.04 °C, compared to 0.65 °C in GISTEMP.

We have verified that the climate states characterized by anomalously low temperatures in the NH are associated with periods of reduced convective mixing in the Labrador Sea, as diagnosed from the local mixed-layer depth (Griffies et al., 2016; not shown). The convective activity is also strongly reduced during the last ~30 years of the pre-industrial control simulation. This suggests that the model suffers from the same instability mechanism active in other EC-Earth3 configurations displaying spurious interdecadal variability in pre-industrial and historical simulations (Döscher et al., in preparation; Parsons et al., 2020). As discussed in Sect. 5, we believe this instability is related to the use of the NEMO3.6 ocean model and the relatively coarse ORCA1 grid (Koenigk et al., 2020).



780 Next, we evaluate the ensemble mean SAT climatology for the last 20 years of the historical simulation (1995–2014) using the
ERA5 reanalysis from the ECMWF (Hersbach et al., 2020; Copernicus Climate Change Service, 2017) as the observational
reference. In Fig. 6 we compare the climatological SAT distributions for all seasons, and for boreal winter (December, January
and February) and summer (June, July and August) separately. The ensemble mean GSAT bias with respect to ERA5 for this
785 period is 0.22 ± 0.18 °C. The mean SAT bias is 1.29 ± 0.05 °C in the Southern Hemisphere and -0.86 ± 0.35 °C in the Northern
Hemisphere. The strongest biases are observed over the Southern Ocean and Antarctica, where temperatures are overestimated
throughout the year. Warm biases also exist in the subtropical marine stratocumulus regions in the eastern South Atlantic and
the eastern North and South Pacific. These biases are common to many climate models and have been attributed to biases in SW cloud
radiative effects (Bodas-Salcedo et al., 2014; 2016, Calisto et al., 2014; Forbes and Ahlgrimm, 2014; Hogan et al., 2017).
790 Temperatures are also overestimated over the Gulf of Alaska and the Bering Sea. Moreover, a warm bias is found in the Kazakhstan
region, mostly during winter. The model underestimates the seasonal cycle in northeastern Siberia, resulting in a warm bias during
winter and a cold bias during summer. Strong cold biases exist during winter over the Arctic Ocean, the Labrador Sea and the
North Atlantic, and also in the Middle East, northern Africa, the United States. As the NH is warming faster than observed, most
of these cold biases tend to be reduced when moving towards the end of the historical period. For instance, restricting the
comparison to the final 10 years of the simulation (2005–2014) reduces the mean bias in the NH to -0.68 ± 0.35 °C.

795
As the historical simulation ensemble underestimates the warming of the NH (Fig. 5b), cold biases in the NH tend to be smaller in
the model's pre-industrial climate. Based on GISTEMP and ERA5, we can estimate that the pre-industrial control simulation
underestimates the mean NH SAT of the late 19th century (strictly 1880–1900) by -0.2 °C. On the other hand, the good agreement
between the simulated and observed SH warming implies that the mean SH SAT bias in the model's pre-industrial climate is
800 similar as for the present day. Our best estimate of this bias based on GISTEMP and ERA5 is 1.2 °C.

4.4 Historical and future perturbation experiments

Figure 7 shows the evolution of the global surface air temperature and net TOA flux from 1850 to 2100 for various CMIP6 and
AerChemMIP experiments. Shown are the annual mean temperature and flux perturbations from a single realization of these
805 experiments (member r1i1p1f1) relative to the pre-industrial means given in Sect. 4.1. The annual global mean tropospheric aerosol
optical depth (AOD) at 550 nm for these simulations is presented in Fig. 8. For the historical period, the CMIP6 historical
simulation is compared with the AerChemMIP hist-piNTCF experiment, in which the emissions of near-term climate forcings
(NTCFs) are kept at pre-industrial levels. NTCFs include aerosols and precursors of aerosols and ozone. Although being an ozone
precursor, the AerChemMIP definition of NTCFs does not include methane. The mean tropospheric AOD at 550 nm is 0.094 in
810 the pre-industrial control simulation and increases to 0.135 at the end of the historical simulation (2005–2014). The hist-piNTCF
experiment yields significantly higher global temperatures than the standard historical simulation from the early 20th century
onwards. The two simulations diverge most rapidly during the 1950s and 1960s, due to a cooling in the historical simulation. The
maximum 10-year rolling mean difference between the two runs is 1.1 °C. However, as we have seen in the previous section, the
model produces large interdecadal variability in the historical period, and the cooling in the 1950s and 1960s is likely a reflection
815 of this. To be able to separate the effects of the NTCF forcings, ensemble simulations are required, which are in production. The
time series of the TOA fluxes show large interannual variability with strong downward excursions after major volcanic eruptions,
reaching 0.7 and 1.0 W m^{-2} at the end of the historical period (2005–2014) in the historical and hist-piNTCF simulations,
respectively.



820 Projections are given for three scenarios, which only differ with respect to assumptions regarding NTCF emissions and methane concentrations. The first scenario experiment (ssp370) follows the standard SSP3-7.0 shared socio-economic pathway from ScenarioMIP (O'Neill et al., 2016), which has relatively high emissions of NTCFs (Gidden et al., 2019). For this scenario EC-Earth3-AerChem produces a global warming of 4.9 °C towards the end of the century (2091–2100). The second is the AerChemMIP experiment ssp370-lowNTCF, which follows the same socio-economic pathway but with reduced emissions of
825 NTCFs (Gidden et al., 2019). This scenario produces enhanced warming, reaching 5.4 °C in the final decade. Finally, in ssp370-lowNTCFCH4 it is assumed that both NTCF emissions and CH₄ concentrations will be reduced compared to ssp370. This scenario produces a significantly lower warming of 4.4 °C. Thus, for these scenarios, reductions in CH₄ concentrations more than offset the enhanced warming due to reductions in NTCF emissions. A more detailed multi-model analysis for these scenario experiments is presented by Allen et al. (2020).

830 5 Discussion and conclusions

This paper documents the global climate model EC-Earth3-AerChem. EC-Earth3-AerChem is a configuration of the EC-Earth3 family of models with interactive tropospheric aerosols and atmospheric chemistry. It uses a coupling between IFS and TM5 to simulate aerosol-radiation and aerosol-cloud interactions as well as chemistry-climate interactions and radiative effects of ozone and methane. We have described the model with a focus on the specific features of EC-Earth3-AerChem compared to the other
835 EC-Earth3 configurations (Döscher et al., in preparation), and on the updates and improvements introduced in TM5 and the TM5-IFS coupled system since the publication of EC-Earth 2.4 (van Noije et al., 2014).

The model's pre-industrial climate was analysed from the available 311 years of the piControl simulation. The net TOA energy imbalance for these years is only $-0.10 \pm 0.25 \text{ W m}^{-2}$ and shows no statistically significant drift. The global surface air temperature
840 (GSAT) is on average $14.05 \pm 0.16 \text{ °C}$ and shows a small linear trend of $-0.075 \pm 0.009 \text{ °C per century}$. Most of this negative trend is due to a low-temperature excursion that appears near the end of the simulated period.

The model's effective equilibrium climate sensitivity (ECS) was robustly estimated at 3.9 °C, using 130 to 150 years of an abrupt-4×CO₂ experiment. This is close to the CMIP6 multi-model mean of $3.7 \pm 1.1 \text{ °C}$ presented by Meehl et al. (2020), but at the high
845 end of the likely range estimated in the recent study by Sherwood et al. (2020). Similarly, the model's transient climate response (TCR) was calculated from a 1pctCO₂ experiment, resulting in a value of 2.1 °C. Again, this is close to the CMIP6 multi-model mean of $2.0 \pm 0.4 \text{ °C}$ from Meehl et al. (2020).

A four-member ensemble of the CMIP6 historical simulation shows large interdecadal variability in Northern Hemisphere and
850 global temperatures during the 20th century, resulting in a large spread among the different members. The ensemble mean GSAT in the last decade of the simulation (2005–2014) is $14.76 \pm 0.19 \text{ °C}$, which is 0.71 °C above the pre-industrial mean. Here the standard deviation indicates the spread in the ensemble.

The evolution of annual mean surface air temperature (SAT) anomalies in the historical ensemble has been compared with
855 observational time series from Cowtan and Way (version 2.0) and GISTEMP (version 4). The model underestimates the warming over the historical period. The ensemble mean temperature change between the second half of the nineteenth century (1850–1900) and the period 2005–2014 is $0.62 \pm 0.23 \text{ °C}$ in the simulations compared to 0.87 and 0.89 °C in the GISTEMP and Cowtan and



Way data sets, respectively. The observed warming of the Southern Hemisphere is well reproduced by the model. For the SH, the ensemble mean SAT anomaly for the period 2005–2014 is 0.69 ± 0.04 °C, compared to 0.65 °C in GISTEMP.

860

The mechanism underlying the spurious interdecadal variability in our simulations is at least partly related to the intermittent nature of the convection in the Labrador Sea, where a reduction or shutdown of the convection during extended periods of time causes anomalously low temperatures in the Northern Hemisphere. Other EC-Earth3 configurations also display spurious interdecadal variability in pre-industrial and historical simulations (Döscher et al., in preparation). We believe this instability is related to the use of NEMO3.6 and the relatively coarse resolution of the ORCA1 grid (Koenigk et al., 2020). Parsons et al. (2020) examined interdecadal GSAT variability in pre-industrial control simulations from 39 CMIP6 models. The six models showing the largest variability are EC-Earth3, BCC-CSM2-MR, CNRM-ESM2-1, EC-Earth3-Veg, CNRM-CM6-1 and IPSL-CM6A-LR. Five of these use NEMO3.6 on the ORCA1 grid (EC-Earth3, EC-Earth3-Veg) or extended ORCA1 (eORCA1) grid (CNRM-ESM2-1, CNRM-CM6-1, IPSL-CM6A-LR). For future research, it would be interesting to consider increasing the resolution of the ocean model in EC-Earth3-AerChem.

865

870

The cooling of the Northern Hemisphere simulated in the 1950s and 1960s may also be caused or enhanced by aerosol effects. To what extent this is the case needs further investigation. Simulations that provide more information on the role of aerosols and their effective radiative forcing contributions are in production.

875

The ensemble mean SAT climatology for the years 1995–2014 has been evaluated against ECMWF’s ERA5 reanalysis. The GSAT bias for this period is 0.22 ± 0.18 °C. The mean SAT bias is 1.29 ± 0.05 °C in the SH and -0.86 ± 0.35 °C in the NH. As the ensemble overestimates the NH warming trends during this period, cold biases in the NH tend to be reduced towards the end of the simulation. For instance, for the last 10 years of the simulation (2005–2014), the mean NH cold bias is reduced to 0.68 ± 0.35 °C.

880

Cold biases in the NH also tend to be smaller in the model’s pre-industrial climate. The pre-industrial control simulation underestimates the mean NH SAT of the late 19th century by approximately -0.2 °C. The good agreement between the simulated and observed warming of the SH over the historical period implies that the mean SH SAT bias in the model’s pre-industrial climate is similar to the present day. Our best estimate of this bias is 1.2 °C.

885

Over the Southern Ocean and Antarctica strong warm biases are found in all seasons. Temperatures are also overestimated in subtropical marine stratocumulus regions. These biases are common to many climate models, including all EC-Earth3 configurations, and have been attributed to biases in SW cloud radiative effects. Modifications in the cloud scheme and the representation of supercooled liquid water made in more recent versions of IFS, including cycle 45r1 (Forbes and Ahlgrimm, 2014; Forbes et al., 2016), together with the introduction of the new ecRad radiation scheme in cycle 43r3 (Hogan et al., 2017) have been shown to substantially reduce these biases.

890

To illustrate the applicability of the model, time series of the GSAT and net TOA flux change relative to their pre-industrial levels have been presented for a number of historical and scenario perturbation experiments from AerChemMIP. For the historical period, the perturbation experiment is one with emissions of near-term climate forcers (NTCFs) fixed to pre-industrial levels. This experiment (hist-piNTCF) produces significantly higher temperatures during the 20th century than the standard historical

895



simulation. For the future period, the standard shared socio-economic pathway SSP3-7.0 from ScenarioMIP has been compared with a scenario with lower NTCF emissions (SSP3-7.0-lowNTCF) and one with both lower NTCF emissions and lower methane concentrations (SSP3-7.0-lowNTCFCH4). For SSP3-7.0, the model projects a global warming at the end of the century (2091–2100) of about 4.9 °C above the pre-industrial level. For the scenario with reduced NTCFs the warming is increased by about 0.5 °C, while for the scenario with both NTCFs and methane reduced the warming is reduced by about 0.5 °C. Note that these estimates are based on a single realization of each experiment. Ensembles required to reduce the impact of internal variability are in production.

905

The representation of aerosols and chemistry has been updated in numerous respects compared to the model version presented by van Noije et al. (2014). The overall result of these changes is a much improved description of in particular aerosol concentrations and optical properties (Bergman et al., in preparation; Gliß et al., 2020; Checa-Garcia et al., 2020). One highlight worth mentioning is that EC-Earth3-AerChem produces substantially higher and more realistic aerosol optical depths (AOD). The mean tropospheric AOD at 550 nm increases from 0.094 in the pre-industrial control simulation to 0.135 in the last decade of the historical simulation (2005–2014). A detailed evaluation of the aerosol simulation is beyond the scope of this paper.

910

The increased complexity from interactive aerosols and atmospheric chemistry comes at the expense of computational performance. The single-core OASIS transfer of spectral fields from IFS to TM5 has been identified as a major bottleneck limiting the scalability of the model. It is expected that a substantial speed-up can be achieved by converting the spectral fields to grid-point fields at the IFS side, enabling domain decomposition and multi-core transfer to TM5. This is planned as part of the model's near-term development.

915

Meanwhile, a number of developments aiming to improve the representation of aerosol and chemical processes are underway. These include the replacement of EQSAM by ISORROPIA II (Fountoukis and Nenes, 2007) or a light version thereof, which is expected to improve the calculation of aerosol water and acidity, as well as the inclusion of coarse-mode nitrate. The MOGUNTIA gas-phase chemistry mechanism has recently been introduced as a more explicit alternative to the current scheme based on CB05 (Myriokefalitakis et al., 2020). A parameterization of marine organic aerosol emissions is also available. Other developments aim to improve the representation of the mineralogical composition and size distribution of dust (Perlwitz et al., 2015a, 2015b; Pérez García-Pando et al., 2016; Adebisi and Kok, 2020) along with the associated effects upon radiation and clouds. Furthermore, it is envisaged that the cloud activation scheme from Abdul-Razzak and Ghan (2000) will be replaced by the more accurate parameterization developed by Morales Betancourt and Nenes (2014), using a more sophisticated turbulence dependent calculation of the updraft velocity.

920

925

930



Code availability

Access to the model code is restricted to institutes that have signed a memorandum of understanding with the EC-Earth community and a software license agreement with the ECMWF. Confidential access to the code can be granted for editors and reviewers.

935 **Data availability**

The CMOR compliant model output files from which the results presented in this article were calculated will be published on the Earth System Grid Federation (ESGF). Specific fields can be made available by the authors upon request.

Author contribution

940 The core team responsible for the development of EC-Earth3-AerChem consisted of TvN, TB and PLS. Other co-authors contributed to the development of specific aspects of the model or parts of the code that are shared with EC-Earth3. PLS, JPK, DOD, and MGA produced the four members of the historical simulation. All other simulations presented in this paper were set up and carried out by PLS. TvN wrote the paper with input from co-authors.

945 **Competing interests**

The authors declare that they have no conflict of interest.

Acknowledgements

TvN, TB and PLS would like to acknowledge funding from the European Union's Horizon 2020 research and innovation programme under grant agreement No 641816 (CRESCENDO). The development of EC-Earth3 and EC-Earth3-AerChem has benefitted from services provided by the IS-ENES3 project, which received funding from the European Union's Horizon 2020 research and innovation programme under grant agreement No 824084. JPK and RM wish to acknowledge CSC – IT Center for Science, Finland, for software support and computational resources. MGA and CPGP acknowledge funding by the European Research Council (grant agreement No. 773051, FRAGMENT), the AXA Research Fund, the Spanish Ministry of Science, 955 Innovation and Universities (RYC-2015-18690 and CGL2017-88911-R), and PRACE and RES for awarding access to MareNostrum at Barcelona Supercomputing Center. RS acknowledges financial support from the strategic research area MERGE (Modelling the Regional and Global Earth system).



References

- 960 Abbatt, J. P. D., Lee, A. K. Y., and Thornton, J. A.: Quantifying trace gas uptake to tropospheric aerosol: recent advances and remaining challenges, *Chem. Soc. Rev.*, 41, 6555–6581, <https://doi.org/10.1039/C2CS35052A>, 2012.
- Abdul-Razzak, H., and Ghan, S. J.: A parameterization of aerosol activation: 2. Multiple aerosol types, *J. Geophys. Res.*, 105, 6837–6844, doi:10.1029/1999JD901161, 2000.
- Adebiyi, A. A., and Kok, J. F.: Climate models miss most of the coarse dust in the atmosphere, *Sci. Adv.*, 6, eaaz9507, doi:10.1126/sciadv.aaz9507, 2020.
- 965 Aiken, A. C., DeCarlo, P. F., Kroll, J. H., Worsnop, D. R., Huffman, J. A., Docherty, K. S., Ulbrich, I. M., Mohr, C., Kimmel, J. R., Sueper, D., Sun, Y., Zhang, Q., Trimborn, A., Northway, M., Ziemann, P. J., Canagaratna, M. R., Onasch, T. B., Alfarra, M. R., Prevot, A. S. H., Dommen, J., Duplissy, J., Metzger, A., Baltensperger, U., and Jimenez, J. L.: O/C and OM/OC ratios of primary, secondary, and ambient organic aerosols with high-resolution time-of-flight aerosol mass spectrometry, *Environ. Sci. Technol.*, 42, 4478–4485, doi:10.1021/es703009q, 2008.
- 970 Albrecht, B. A.: Aerosols, cloud microphysics, and fractional cloudiness, *Science*, 245, 1227–1230, doi:10.1126/science.245.4923.1227, 1989.
- Allen, R., Horowitz, L., Naik, V., Oshima, N., O'Connor, F., Turnock, S., Shim, S., Le Sager, P., van Noije, T., Tsigaridis, K., Bauer, S., Sentman, L., John, J., Broderick, C., Deushi, M., Folberth, G., Fujimori, S., Collins, W.: Significant climate benefits from near-term climate forcer mitigation in spite of aerosol reductions, *Environ. Res. Lett.*, submitted, 2020.
- 975 Ammann, M., Cox, R. A., Crowley, J. N., Jenkin, M. E., Mellouki, A., Rossi, M. J., Troe, J., and Wallington, T. J.: Evaluated kinetic and photochemical data for atmospheric chemistry: Volume VI – heterogeneous reactions with liquid substrates, *Atmos. Chem. Phys.*, 13, 8045–8228, <https://doi.org/10.5194/acp-13-8045-2013>, 2013.
- Andrews, T., Gregory, J. M., Webb, M. J., and Taylor, K. E.: Forcing, feedbacks and climate sensitivity in CMIP5 coupled atmosphere-ocean climate models, *Geophys. Res. Lett.*, 39, L09712, doi:10.1029/2012GL051607, 2012.
- 980 Balaji, V., Maiconnave, E., Zadeh, N., Lawrence, B. N., Biercamp, J., Fladrich, U., Aloisio, G., Benson, R., Caubel, A., Durachta, J., Foujols, M.-A., Lister, G., Mocavero, S., Underwood, S., and Wright, G.: CPMIP: measurements of real computational performance of Earth system models in CMIP6, *Geosci. Model Dev.*, 10, 19–34, <https://doi.org/10.5194/gmd-10-19-2017>, 2017.
- 985 Balsamo, G., Beljaars, A., Scipal, K., Viterbo, P., van den Hurk, B., Hirschi, M., and Betts, A. K.: A revised hydrology for the ECMWF model: Verification from field site to terrestrial water storage and impact in the Integrated Forecast System, *J. Hydrometeorol.*, 10, 623–643, <https://doi.org/10.1175/2008JHM1068.1>, 2009.
- Bándá, N., Krol, M., van Noije, T., van Weele, M., Williams, J. E., Le Sager, P., Niemeier, U., Thomason, L., and Röckmann, T.: The effect of stratospheric sulfur from Mount Pinatubo on tropospheric oxidizing capacity and methane, *J. Geophys. Res.*, 120, 2014JD022137, doi:10.1002/2014JD022137, 2014.
- 990 Bechtold, P., Semane, N., Lopez, P., Chaboureaud, J., Beljaars, A., and Bormann, N.: Representing equilibrium and nonequilibrium convection in large-scale models, *J. Atmos. Sci.*, 71, 734–753, <https://doi.org/10.1175/JAS-D-13-0163.1>, 2014.
- Bergman, T., Makkonen, R., Schrödner, R., Swietlicki, E., Phillips, V. T. J., Le Sager, P., and van Noije, T.: Description and evaluation of a secondary organic aerosol and new particle formation scheme within TM5-MP v1.1, *Geosci. Model Dev.*, in preparation.
- 995 Bodas-Salcedo, A., Williams, K. D., Ringer, M. A., Beau, I., Cole, J. N. S., Dufresne, J.-L., Koshiro, T., Stevens, B., Wang, Z., and Yokohata, T.: Origins of the solar radiation biases over the Southern Ocean in CFMIP2 models, *J. Climate*, 27, 41–56, <https://doi.org/10.1175/JCLI-D-13-00169.1>, 2014.
- 1000 Bodas-Salcedo, A., Hill, P. G., Furtado, K., Williams, K. D., Field, P. R., Manners, J. C., Hyder, P., and Kato, S.: Large contribution of supercooled liquid clouds to the solar radiation budget of the Southern Ocean. *J. Climate*, 29, 4213–4228, <https://doi.org/10.1175/JCLI-D-15-0564.1>, 2016.



- 1005 Bond, T. C., Doherty, S. J., Fahey, D. W., Forster, P. M., Bernsten, T., DeAngelo, B. J., Flanner, M. G., Ghan, S., Kärcher, B., Koch, D., Kinne, S., Kondo, Y., Quinn, P. K., Sarofim, M. C., Schultz, M. G., Schulz, M., Venkataraman, C., Zhang, H., Zhang, S., Bellouin, N., Guttikunda, S. K., Hopke, P. K., Jacobson, M. Z., Kaiser, J. W., Klimont, Z., Lohmann, U., Schwarz, J. P., Shindell, D., Storelvmo, T., Warren, S. G., and Zender, C. S.: Bounding the role of black carbon in the climate system: A scientific assessment, *J. Geophys. Res. Atmos.*, 118, 5380–5552, doi:10.1002/jgrd.50171, 2013.
- 1010 Bond, T. C., and Bergstrom, R. W.: Light absorption by carbonaceous particles: An investigative review, *Aerosol Sci. Technol.*, 40, 27–67, doi:10.1080/02786820500421521, 2006.
- 1015 Bourgeois, Q., and Bey, I.: Pollution transport efficiency toward the Arctic: Sensitivity to aerosol scavenging and source regions, *J. Geophys. Res.*, 116, D08213, doi:10.1029/2010JD015096, 2011.
- aan de Brugh, J. M. J., Schaap, M., Vignati, E., Dentener, F., Kahnert, M., Sofiev, M., Huijnen, V., and Krol, M. C.: The European aerosol budget in 2006, *Atmos. Chem. Phys.*, 11, 1117–1139, <https://doi.org/10.5194/acp-11-1117-2011>, 2011.
- 1020 de Bruine, M., Krol, M., van Noije, T., Le Sager, P., and Röckmann, T.: The impact of precipitation evaporation on the atmospheric aerosol distribution in EC-Earth v3.2.0, *Geosci. Model Dev.*, 11, 1443–1465, <https://doi.org/10.5194/gmd-11-1443-2018>, 2018.
- Calisto, M., Folini, D., Wild, M., and Bengtsson, L.: Cloud radiative forcing intercomparison between fully coupled CMIP5 models and CERES satellite data, *Ann. Geophys.*, 32, 793–807, <https://doi.org/10.5194/angeo-32-793-2014>, 2014.
- 1025 Checa-Garcia, R., Hegglin, M. I., Kinnison, D., Plummer, D. A., & Shine, K. P.: Historical tropospheric and stratospheric ozone radiative forcing using the CMIP6 database. *Geophys. Res. Lett.*, 45, 3264–3273. <https://doi.org/10.1002/2017GL076770>, 2018.
- 1030 Checa-Garcia, R., Balkanski, Y., Albani, S., Bergman, T., Carslaw, K., Cozic, A., Dearden, C., Marticorena, B., Michou, M., van Noije, T., Nabat, P., O'Connor, F., Olivie, D., Prospero, J. M., Le Sager, P., Schulz, M., and Scott, C.: Evaluation of natural aerosols in CRESCENDO-ESMs: Mineral Dust, *Atmos. Chem. Phys. Discuss.*, <https://doi.org/10.5194/acp-2020-1147>, in review, 2020.
- 1035 Cheng, T., Peng, Y., Feichter, J., and Tegen, I.: An improvement on the dust emission scheme in the global aerosol-climate model ECHAM5-HAM, *Atmos. Chem. Phys.*, 8, 1105–1117, <https://doi.org/10.5194/acp-8-1105-2008>, 2008.
- Collins, W. J., Lamarque, J.-F., Schulz, M., Boucher, O., Eyring, V., Hegglin, M. I., Maycock, A., Myhre, G., Prather, M., Shindell, D., and Smith, S. J.: AerChemMIP: quantifying the effects of chemistry and aerosols in CMIP6, *Geosci. Model Dev.*, 10, 585–607, <https://doi.org/10.5194/gmd-10-585-2017>, 2017.
- 1040 Copernicus Climate Change Service (C3S): ERA5: Fifth generation of ECMWF atmospheric reanalyses of the global climate, Copernicus Climate Change Service Climate Data Store (CDS), <https://cds.climate.copernicus.eu/cdsapp#!/home>, accessed 17 September 2020, 2017.
- 1045 Cowtan, K., Hausfather, Z., Hawkins, E., Jacobs, P., Mann, M. E., Miller, S. K., Steinman, B. A., Stolpe, M. B., and Way, R. G.: Robust comparison of climate models with observations using blended land air and ocean sea surface temperatures, *Geophys. Res. Lett.*, 42, 6526–6534, doi:10.1002/2015GL064888, 2015.
- 1050 Cowtan, K. and Way, R. G.: Coverage bias in the HadCRUT4 temperature series and its impact on recent temperature trends, *Q.J.R. Meteorol. Soc.*, 140, 1935–1944. doi:10.1002/qj.2297, 2014.
- Cowtan, K. and Way, R. G.: HadCRUT4 infilled by kriging, version 2.0, University of York, Department of Chemistry, <https://www-users.york.ac.uk/~kdc3/papers/coverage2013/series.html>, accessed 17 September 2020.
- 1055 Craig, A., Valcke, S., Coquart, L.: Development and performance of a new version of the OASIS coupler, OASIS3-MCT_3.0, *Geosci. Mod. Dev.*, 10, 3297–3308, doi:10.5194/gmd-10-3297-2017, 2017.
- 1060 Croft, B., Lohmann, U., Martin, R. V., Stier, P., Wurzler, S., Feichter, J., Posselt, R., and Ferrachat, S.: Aerosol size-dependent below-cloud scavenging by rain and snow in the ECHAM5-HAM, *Atmos. Chem. Phys.*, 9, 4653–4675, <https://doi.org/10.5194/acp-9-4653-2009>, 2009.



- Croft, B., Lohmann, U., Martin, R. V., Stier, P., Wurzler, S., Feichter, J., Hoose, C., Heikkilä, U., van Donkelaar, A., and Ferrachat, S.: Influences of in-cloud aerosol scavenging parameterizations on aerosol concentrations and wet deposition in ECHAM5-HAM, *Atmos. Chem. Phys.*, 10, 1511–1543, <https://doi.org/10.5194/acp-10-1511-2010>, 2010.
- 1065 Cross, E. S., Slowik, J. G., Davidovits, P., Allan, J. D., Worsnop, D. R., Jayne, J. T., Lewis, D. K., Canagaratna, M., and Onasch, T. B.: Laboratory and ambient particle density determinations using light scattering in conjunction with aerosol mass spectrometry, *Aerosol Sci. Technol.*, 41, 343–359, doi:10.1080/02786820701199736, 2007.
- 1070 Crowley, J. N., Ammann, M., Cox, R. A., Hynes, R. G., Jenkin, M. E., Mellouki, A., Rossi, M. J., Troe, J., and Wallington, T. J.: Evaluated kinetic and photochemical data for atmospheric chemistry: Volume V – heterogeneous reactions on solid substrates, *Atmos. Chem. Phys.*, 10, 9059–9223, <https://doi.org/10.5194/acp-10-9059-2010>, 2010.
- 1075 Davini, P., von Hardenberg, J., Corti, S., Christensen, H. M., Juricke, S., Subramanian, A., Watson, P. A. G., Weisheimer, A., and Palmer, T. N.: Climate SPHINX: evaluating the impact of resolution and stochastic physics parameterisations in the EC-Earth global climate model, *Geosci. Model Dev.*, 10, 1383–1402, <https://doi.org/10.5194/gmd-10-1383-2017>, 2017.
- 1080 Dee, D. P., Uppala, S. M., Simmons, A. J., Berrisford, P., Poli, P., Kobayashi, S., Andrae, U., Balmaseda, M. A., Balsamo, G., Bauer, P., Bechtold, P., Beljaars, A. C. M., van de Berg, L., Bidlot, J., Bormann, N., Delsol, C., Dragani, R., Fuentes, M., Geer, A. J., Haimberger, L., Healy, S. B., Hersbach, H., Hólm, E. V., Isaksen, I., Kållberg, P., Köhler, M., Matricardi, M., McNally, A. P., Monge-Sanz, B. M., Morcrette, J.-J., Park, B.-K., Peubey, C., de Rosnay, P., Tavolato, C., Thépaut, J.-N. and Vitart, F.: The ERA-Interim reanalysis: configuration and performance of the data assimilation system. *Q. J. R. Meteorol. Soc.*, 137, 553–597, doi:10.1002/qj.828, 2011.
- 1085 Dentener, F., Kinne, S., Bond, T., Boucher, O., Cofala, J., Generoso, S., Ginoux, P., Gong, S., Hoelzemann, J. J., Ito, A., Marelli, L., Penner, J. E., Putaud, J.-P., Textor, C., Schulz, M., van der Werf, G. R., and Wilson, J.: Emissions of primary aerosol and precursor gases in the years 2000 and 1750 prescribed data-sets for AeroCom, *Atmos. Chem. Phys.*, 6, 4321–4344, <https://doi.org/10.5194/acp-6-4321-2006>, 2006.
- 1090 Diamantakis, M. and Flemming, J.: Global mass fixer algorithms for conservative tracer transport in the ECMWF model, *Geosci. Model Dev.*, 7, 965–979, <https://doi.org/10.5194/gmd-7-965-2014>, 2014.
- Döscher, R., von Hardenberg, J., Wyser, K., et al.: The Community Earth System Model EC-Earth for collaborative climate research, *Geosci. Model Dev.*, in preparation.
- 1095 Evans, M. J., and Jacob, D. J.: Impact of new laboratory studies of N₂O₅ hydrolysis on global model budgets of tropospheric nitrogen oxides, ozone, and OH, *Geophys. Res. Lett.*, 32, L09813, doi:10.1029/2005GL022469, 2005.
- 1100 Eyring, V., Bony, S., Meehl, G. A., Senior, C. A., Stevens, B., Stouffer, R. J., and Taylor, K. E.: Overview of the Coupled Model Intercomparison Project Phase 6 (CMIP6) experimental design and organization, *Geosci. Model Dev.*, 9, 1937–1958, <https://doi.org/10.5194/gmd-9-1937-2016>, 2016.
- 1105 Feng, L., Smith, S. J., Braun, C., Crippa, M., Gidden, M. J., Hoesly, R., Klimont, Z., van Marle, M., van den Berg, M., and van der Werf, G. R.: The generation of gridded emissions data for CMIP6, *Geosci. Model Dev.*, 13, 461–482, <https://doi.org/10.5194/gmd-13-461-2020>, 2020.
- Fountoukis, C. and Nenes, A.: ISORROPIA II: a computationally efficient thermodynamic equilibrium model for K⁺-Ca²⁺-Mg²⁺-NH₄⁺-Na⁺-SO₄²⁻-NO₃⁻-Cl⁻-H₂O aerosols, *Atmos. Chem. Phys.*, 7, 4639–4659, <https://doi.org/10.5194/acp-7-4639-2007>, 2007.
- 1110 Forbes, R. M., and Ahlgrimm, M.: On the representation of high-latitude boundary layer mixed-phase cloud in the ECMWF global model, *Mon. Wea. Rev.*, 142, 3425–3445, <https://doi.org/10.1175/MWR-D-13-00325.1>, 2014.
- 1115 Forbes, R., Geer, A., Lonitz, K., and Ahlgrimm, M.: Reducing systematic error in cold-air outbreaks, *ECMWF Newsletter No. 146*, 17–22, 2016.
- Ghan, S. J.: Technical Note: Estimating aerosol effects on cloud radiative forcing, *Atmos. Chem. Phys.*, 13, 9971–9974, <https://doi.org/10.5194/acp-13-9971-2013>, 2013.
- 1120 Gidden, M. J., Riahi, K., Smith, S. J., Fujimori, S., Luderer, G., Kriegler, E., van Vuuren, D. P., van den Berg, M., Feng, L., Klein, D., Calvin, K., Doelman, J. C., Frank, S., Fricko, O., Harmsen, M., Hasegawa, T., Havlik, P., Hilaire, J., Hoesly, R.,



- Horing, J., Popp, A., Stehfest, E., and Takahashi, K.: Global emissions pathways under different socioeconomic scenarios for use in CMIP6: a dataset of harmonized emissions trajectories through the end of the century, *Geosci. Model Dev.*, 12, 1443–1475, <https://doi.org/10.5194/gmd-12-1443-2019>, 2019.
- 1125 GISTEMP Team: GISS Surface Temperature Analysis (GISTEMP), version 4, NASA Goddard Institute for Space Studies, <https://data.giss.nasa.gov/gistemp/>, accessed 17 September 2020.
- 1130 Gliß, J., Mortier, A., Schulz, M., Andrews, E., Balkanski, Y., Bauer, S. E., Benedictow, A. M. K., Bian, H., Checa-Garcia, R., Chin, M., Ginoux, P., Griesfeller, J. J., Heckel, A., Kipling, Z., Kirkevåg, A., Kokkola, H., Laj, P., Le Sager, P., Lund, M. T., Lund Myhre, C., Matsui, H., Myhre, G., Neubauer, D., van Noije, T., North, P., Olivie, D. J. L., Sogacheva, L., Takemura, T., Tsigaridis, K., and Tsyro, S. G.: Multi-model evaluation of aerosol optical properties in the AeroCom phase III Control experiment, using ground and space based columnar observations from AERONET, MODIS, AATSR and a merged satellite product as well as surface in-situ observations from GAW sites, *Atmos. Chem. Phys. Discuss.*, <https://doi.org/10.5194/acp-2019-1214>, accepted, 2020.
- 1135 Gong, S. L.: A parameterization of sea-salt aerosol source function for sub- and super-micron particles, *Global Biogeochem. Cycles*, 17, 1097, doi:10.1029/2003GB002079, 2003.
- 1140 Gregory, J. M., Ingram, W. J., Palmer, M. A., Jones, G. S., Stott, P. A., Thorpe, R. B., Lowe, J. A., Johns, T. C., and Williams, K. D.: A new method for diagnosing radiative forcing and climate sensitivity, *Geophys. Res. Lett.*, 31, L03205, doi:10.1029/2003GL018747, 2004.
- 1145 Griffies, S. M., Danabasoglu, G., Durack, P. J., Adcroft, A. J., Balaji, V., Böning, C. W., Chassignet, E. P., Curchitser, E., Deshayes, J., Drange, H., Fox-Kemper, B., Gleckler, P. J., Gregory, J. M., Haak, H., Hallberg, R. W., Heimbach, P., Hewitt, H. T., Holland, D. M., Ilyina, T., Jungclaus, J. H., Komuro, Y., Krasting, J. P., Large, W. G., Marsland, S. J., Masina, S., McDougall, T. J., Nurser, A. J. G., Orr, J. C., Pirani, A., Qiao, F., Stouffer, R. J., Taylor, K. E., Treguier, A. M., Tsujino, H., Uotila, P., Valdivieso, M., Wang, Q., Winton, M., and Yeager, S. G.: OMIP contribution to CMIP6: experimental and diagnostic protocol for the physical component of the Ocean Model Intercomparison Project, *Geosci. Model Dev.*, 9, 3231–3296, <https://doi.org/10.5194/gmd-9-3231-2016>, 2016.
- 1150 Grooß, J.-U. and Russell III, J. M.: Technical note: A stratospheric climatology for O₃, H₂O, CH₄, NO_x, HCl and HF derived from HALOE measurements, *Atmos. Chem. Phys.*, 5, 2797–2807, <https://doi.org/10.5194/acp-5-2797-2005>, 2005.
- 1155 Haarsma, R., Acosta, M., Bakhshi, R., Bretonnière, P.-A., Caron, L.-P., Castrillo, M., Corti, S., Davini, P., Exarchou, E., Fabiano, F., Fladrich, U., Fuentes Franco, R., García-Serrano, J., von Hardenberg, J., Koenigk, T., Levine, X., Meccia, V. L., van Noije, T., van den Oord, G., Palmeiro, F. M., Rodrigo, M., Ruprich-Robert, Y., Le Sager, P., Tourigny, E., Wang, S., van Weele, M., and Wyser, K.: HighResMIP versions of EC-Earth: EC-Earth3P and EC-Earth3P-HR – description, model computational performance and basic validation, *Geosci. Model Dev.*, 13, 3507–3527, <https://doi.org/10.5194/gmd-13-3507-2020>, 2020.
- 1160 Hazeleger, W., Severijns, C., Semmler, T., Ştefănescu, S., Yang, S., Wang, X., Wyser, K., Dutra, E., Baldasano, J. M., Bintanja, R., Bougeault, P., Caballero, R., Ekman, A. M. L., Christensen, J. H., van den Hurk, B., Jimenez, P., Jones, C., Källberg, P., Koenigk, T., McGrath, R., Miranda, P., van Noije, T., Palmer, T., Parodi, J. A., Schmith, T., Selten, F., Storelvmo, T., Sterl, A., Tapamo, H., Vancoppenolle, M., Viterbo, P., and Willén, U.: EC-Earth: a seamless earth-system prediction approach in action, *Bull. Am. Meteorol. Soc.*, 91, 1357–1363, 2010.
- 1165 Hazeleger, W., Wang, X., Severijns, C., Ştefănescu, S., Bintanja, R., Sterl, A., Wyser, K., Semmler, T., Yang, S., van den Hurk, B., van Noije, T., van der Linden, E., and van der Wiel, K.: EC-Earth V2.2: description and validation of a new seamless earth system prediction model, *Clim. Dynam.*, 39, 2611–2629, 2012.
- 1170 Hersbach, H., Bell, B., Berrisford, P., Hirahara, S., Horányi, A., Muñoz-Sabater, J., Nicolas, J., Peubey, C., Radu, R., Schepers, D., Simmons, A., Soci, C., Abdalla, S., Abellan, X., Balsamo, G., Bechtold, P., Biavati, G., Bidlot, J., Bonavita, M., De Chiara, G., Dahlgren, P., Dee, D., Diamantakis, M., Dragani, R., Flemming, J., Forbes, R., Fuentes, M., Geer, A., Haimberger, L., Healy, S., Hogan, R. J., Hólm, E., Janisková, M., Keeley, S., Laloyaux, P., Lopez, P., Lupu, C., Radnoti, G., de Rosnay, P., Rozum, I., Vamborg, F., Villaume, S., and Thépaut, J.-N.: The ERA5 global reanalysis. *Q. J. R. Meteorol. Soc.*, 1–51, <https://doi.org/10.1002/qj.3803>, 2020.
- Hess, M., Koepke, P., Schult, I.: Optical Properties of Aerosols and Clouds: The Software Package OPAC, *Bull. Amer. Meteor. Soc.*, 79, 831–844, [https://doi.org/10.1175/1520-0477\(1998\)079<0831:OPOAAC>2.0.CO;2](https://doi.org/10.1175/1520-0477(1998)079<0831:OPOAAC>2.0.CO;2), 1998.



- 1175 Hewitt, H. T., Copley, D., Culverwell, I. D., Harris, C. M., Hill, R. S. R., Keen, A. B., McLaren, A. J., and Hunke, E. C.: Design and implementation of the infrastructure of HadGEM3: the next-generation Met Office climate modelling system, *Geosci. Model Dev.*, 4, 223–253, <https://doi.org/10.5194/gmd-4-223-2011>, 2011.
- 1180 Hoesly, R. M., Smith, S. J., Feng, L., Klimont, Z., Janssens-Maenhout, G., Pitkanen, T., Seibert, J. J., Vu, L., Andres, R. J., Bolt, R. M., Bond, T. C., Dawidowski, L., Kholod, N., Kurokawa, J.-I., Li, M., Liu, L., Lu, Z., Moura, M. C. P., O'Rourke, P. R., and Zhang, Q.: Historical (1750–2014) anthropogenic emissions of reactive gases and aerosols from the Community Emissions Data System (CEDS), *Geosci. Model Dev.*, 11, 369–408, <https://doi.org/10.5194/gmd-11-369-2018>, 2018.
- Hogan, R., Ahlgrim, M., Balsamo, G., Beljaars, A., Berrisford, P., Bozzo, A., Di Giuseppe, F., Forbes, R. M., Haiden, T., Lang, S., Mayer, M., Polichtchouk, I., Sandu, I., Vitart, F., and Wedi, N.: Radiation in numerical weather prediction, ECMWF Technical Memorandum No. 816, 49 pp., <https://doi.org/10.21957/2bd5dkj8x>, 2017.
- 1185 Huijnen, V., Williams, J. E., and Flemming, J.: Modeling global impacts of heterogeneous loss of HO₂ on cloud droplets, ice particles and aerosols, *Atmos. Chem. Phys. Discuss.*, 14, 8575–8632, <https://doi.org/10.5194/acpd-14-8575-2014>, 2014.
- 1190 Huijnen, V., Williams, J., van Weele, M., van Noije, T., Krol, M., Dentener, F., Segers, A., Houweling, S., Peters, W., de Laat, J., Boersma, F., Bergamaschi, P., van Velthoven, P., Le Sager, P., Eskes, H., Alkemade, F., Scheele, R., Nédélec, P., and Pätz, H.-W.: The global chemistry transport model TM5: description and evaluation of the tropospheric chemistry version 3.0, *Geosci. Model Dev.*, 3, 445–473, <https://doi.org/10.5194/gmd-3-445-2010>, 2010.
- 1195 Hurr, G. C., Chini, L., Sahajpal, R., Frohling, S., Bodirsky, B. L., Calvin, K., Doelman, J. C., Fisk, J., Fujimori, S., Klein Goldeewijk, K., Hasegawa, T., Havlik, P., Heinemann, A., Humenöder, F., Jungclaus, J., Kaplan, J. O., Kennedy, J., Krisztin, T., Lawrence, D., Lawrence, P., Ma, L., Mertz, O., Pongratz, J., Popp, A., Poulter, B., Riahi, K., Shevliakova, E., Stehfest, E., Thornton, P., Tubiello, F. N., van Vuuren, D. P., and Zhang, X.: Harmonization of global land use change and management for the period 850–2100 (LUH2) for CMIP6, *Geosci. Model Dev.*, 13, 5425–5464, <https://doi.org/10.5194/gmd-13-5425-2020>, 2020.
- Jacob, D. J.: Heterogeneous chemistry and tropospheric ozone, *Atmos. Environ.*, 34, 2131–2159, [https://doi.org/10.1016/S1352-2310\(99\)00462-8](https://doi.org/10.1016/S1352-2310(99)00462-8), 2000.
- 1200 Jaeglé, L., Quinn, P. K., Bates, T. S., Alexander, B., and Lin, J.-T.: Global distribution of sea salt aerosols: new constraints from in situ and remote sensing observations, *Atmos. Chem. Phys.*, 11, 3137–3157, <https://doi.org/10.5194/acp-11-3137-2011>, 2011.
- Janhäll, S., Andreae, M. O., and Pöschl, U.: Biomass burning aerosol emissions from vegetation fires: particle number and mass emission factors and size distributions, *Atmos. Chem. Phys.*, 10, 1427–1439, <https://doi.org/10.5194/acp-10-1427-2010>, 2010.
- Jung, J. G., Pandis, S. N., and Adams, P. J.: Evaluation of nucleation theories in a sulfur-rich environment, *Aerosol Sci. Technol.*, 42, 495–504, doi:10.1080/02786820802187085, 2008.
- 1205 Kerminen, V.-M., and Kulmala, M.: Analytical formulae connecting the “real” and the “apparent” nucleation rate and the nuclei number concentration for atmospheric nucleation events, *J. Aerosol Sci.*, 33, 609–622, [https://doi.org/10.1016/S0021-8502\(01\)00194-X](https://doi.org/10.1016/S0021-8502(01)00194-X), 2002.
- 1210 Kerminen, V.-M., Petäjä, T., Manninen, H. E., Paasonen, P., Nieminen, T., Sipilä, M., Junninen, H., Ehn, M., Gagné, S., Laakso, L., Riipinen, I., Vehkamäki, H., Kurten, T., Ortega, I. K., Dal Maso, M., Brus, D., Hyvärinen, A., Lihavainen, H., Leppä, J., Lehtinen, K. E. J., Mirme, A., Mirme, S., Hörrak, U., Berndt, T., Stratmann, F., Birmili, W., Wiedensohler, A., Metzger, A., Dommen, J., Baltensperger, U., Kiendler-Scharr, A., Mentel, T. F., Wildt, J., Winkler, P. M., Wagner, P. E., Petzold, A., Minikin, A., Plass-Dülmer, C., Pöschl, U., Laaksonen, A., and Kulmala, M.: Atmospheric nucleation: highlights of the EUCAARI project and future directions, *Atmos. Chem. Phys.*, 10, 10829–10848, <https://doi.org/10.5194/acp-10-10829-2010>, 2010.
- 1215 Kodros, J. K., Scott, C. E., Farina, S. C., Lee, Y. H., L'Orange, C., Volckens, J., and Pierce, J. R.: Uncertainties in global aerosols and climate effects due to biofuel emissions, *Atmos. Chem. Phys.*, 15, 8577–8596, <https://doi.org/10.5194/acp-15-8577-2015>, 2015.
- 1220 Koenigk, T., Fuentes-Franco, R., Meccia, V., Gutjahr, O., Jackson, L. C., New, A. L., Ortega, P., Roberts, C., Roberts, M., Arsouze, T., Iovino, D., Moine, M.-P., and Sein, D. V.: Deep water formation in the North Atlantic Ocean in high resolution global coupled climate models, *Ocean Sci. Discuss.*, <https://doi.org/10.5194/os-2020-41>, 2020.



- Krol, M., Houweling, S., Bregman, B., van den Broek, M., Segers, A., van Velthoven, P., Peters, W., Dentener, F., and Bergamaschi, P.: The two-way nested global chemistry-transport zoom model TM5: algorithm and applications, *Atmos. Chem. Phys.*, 5, 417–432, <https://doi.org/10.5194/acp-5-417-2005>, 2005.
- 1225 Kuwata, M., Zorn, S. R., and Martin, S. T.: Using elemental ratios to predict the density of organic material composed of carbon, hydrogen, and oxygen, *Environ. Sci. Technol.*, 46, 787–794, [doi:10.1021/es202525q](https://doi.org/10.1021/es202525q), 2012.
- Lana, A., Bell, T. G., Simó, R., Vallina, S. M., Ballabrera-Poy, J., Kettle, A. J., Dachs, J., Bopp, L., Saltzman, E. S., Stefels, J., Johnson, J. E., and Liss, P. S.: An updated climatology of surface dimethylsulfide concentrations and emission fluxes in the global ocean, *Global Biogeochem. Cycles*, 25, GB1004, [doi:10.1029/2010GB003850](https://doi.org/10.1029/2010GB003850), 2011.
- 1230 Lee, B. H., Kostenidou, E., Hildebrandt, L., Riipinen, I., Engelhart, G. J., Mohr, C., DeCarlo, P. F., Mihalopoulos, N., Prevot, A. S. H., Baltensperger, U., and Pandis, S. N.: Measurement of the ambient organic aerosol volatility distribution: application during the Finokalia Aerosol Measurement Experiment (FAME-2008), *Atmos. Chem. Phys.*, 10, 12149–12160, <https://doi.org/10.5194/acp-10-12149-2010>, 2010.
- Lenßen, N., G. Schmidt, J. Hansen, M. Menne, A. Persin, R. Ruedy, and D. Zyss: Improvements in the GISTEMP uncertainty model, *J. Geophys. Res. Atmos.*, 124, 6307–6326, [doi:10.1029/2018JD029522](https://doi.org/10.1029/2018JD029522), 2019.
- 1235 Li, X., Wang, S., Duan, L., Hao, J., and Nie, Y.: Carbonaceous aerosol emissions from household biofuel combustion in China, *Environ. Sci. Technol.*, 43, 6076–6081, <https://doi.org/10.1021/es803330j>, 2009.
- Lin, Y., Farley, R. D., and Orville, H. D.: Bulk parameterization of the snow field in a cloud model, *J. Climate Appl. Meteor.*, 22, 1065–1092, [https://doi.org/10.1175/1520-0450\(1983\)022<1065:BPOTSF>2.0.CO;2](https://doi.org/10.1175/1520-0450(1983)022<1065:BPOTSF>2.0.CO;2), 1983.
- 1240 Madec, G., and Imbard, M.: A global ocean mesh to overcome the North Pole singularity, *Clim. Dynam.*, 12, 381–388, <https://doi.org/10.1007/BF00211684>, 1996.
- Madec, G., and the NEMO team: NEMO ocean engine – version 3.6 stable, Note du Pôle de modélisation de l’Institut Pierre-Simon Laplace (IPSL), France, Note No. 27, 401 pp., 2015.
- 1245 van Marle, M. J. E., Kloster, S., Magi, B. I., Marlon, J. R., Daniau, A.-L., Field, R. D., Arneeth, A., Forrest, M., Hantson, S., Kehrwald, N. M., Knorr, W., Lasslop, G., Li, F., Mangeon, S., Yue, C., Kaiser, J. W., and van der Werf, G. R.: Historic global biomass burning emissions for CMIP6 (BB4CMIP) based on merging satellite observations with proxies and fire models (1750–2015), *Geosci. Model Dev.*, 10, 3329–3357, <https://doi.org/10.5194/gmd-10-3329-2017>, 2017.
- Mårtensson, E. M., Nilsson, E. D., de Leeuw, G., Cohen, L. H., and Hansson, H.-C.: Laboratory simulations and parameterization of the primary marine aerosol production, *J. Geophys. Res.*, 108, 4297, [doi:10.1029/2002JD002263](https://doi.org/10.1029/2002JD002263), 2003.
- 1250 Marticorena, B., and Bergametti, G.: Modeling the atmospheric dust cycle: 1. Design of a soil-derived dust emission scheme, *J. Geophys. Res.*, 100, 16415–16430, [doi:10.1029/95JD00690](https://doi.org/10.1029/95JD00690), 1995.
- Martin, G. M., Johnson, D. W., and Spice, A.: The measurement and parameterization of effective radius of droplets in warm stratocumulus clouds, *J. Atmos. Sci.*, 51, 1823–1842, [https://doi.org/10.1175/1520-0469\(1994\)051<1823:TMAPOE>2.0.CO;2](https://doi.org/10.1175/1520-0469(1994)051<1823:TMAPOE>2.0.CO;2), 1994.
- 1255 Matthes, K., Funke, B., Andersson, M. E., Barnard, L., Beer, J., Charbonneau, P., Clilverd, M. A., Dudok de Wit, T., Haberreiter, M., Hendry, A., Jackman, C. H., Kretzschmar, M., Kruschke, T., Kunze, M., Langematz, U., Marsh, D. R., Maycock, A. C., Misios, S., Rodger, C. J., Scaife, A. A., Seppälä, A., Shangguan, M., Sinnhuber, M., Tourpali, K., Usoskin, I., van de Kamp, M., Verronen, P. T., and Versick, S.: Solar forcing for CMIP6 (v3.2), *Geosci. Model Dev.*, 10, 2247–2302, <https://doi.org/10.5194/gmd-10-2247-2017>, 2017.
- 1260 Mayol-Bracero, O. L., Guyon, P., Graham, B., Roberts, G., Andreae, M. O., Decesari, S., Facchini, M. C., Fuzzi, S., and Artaxo, P.: Water-soluble organic compounds in biomass burning aerosols over Amazonia, 2, Apportionment of the chemical composition and importance of the polyacidic fraction, *J. Geophys. Res.*, 107, 8091, [doi:10.1029/2001JD000522](https://doi.org/10.1029/2001JD000522), 2002.
- Meehl, G. A., Senior, C. A., Eyring, V., Flato, G., Lamarque, J.-F., Stouffer, R. J., Taylor, K. E., and Schlund, M.: Context for interpreting equilibrium climate sensitivity and transient climate response from the CMIP6 Earth system models, *Sci. Adv.*, 6, <https://doi.org/10.1126/sciadv.aba1981>, 2020.



- 1265 Meinshausen, M., Vogel, E., Nauels, A., Lorbacher, K., Meinshausen, N., Etheridge, D. M., Fraser, P. J., Montzka, S. A., Rayner, P. J., Trudinger, C. M., Krummel, P. B., Beyerle, U., Canadell, J. G., Daniel, J. S., Enting, I. G., Law, R. M., Lunder, C. R., O'Doherty, S., Prinn, R. G., Reimann, S., Rubino, M., Velders, G. J. M., Vollmer, M. K., Wang, R. H. J., and Weiss, R.: Historical greenhouse gas concentrations for climate modelling (CMIP6), *Geosci. Model Dev.*, 10, 2057–2116, <https://doi.org/10.5194/gmd-10-2057-2017>, 2017.
- 1270 Meinshausen, M., Nicholls, Z. R. J., Lewis, J., Gidden, M. J., Vogel, E., Freund, M., Beyerle, U., Gessner, C., Nauels, A., Bauer, N., Canadell, J. G., Daniel, J. S., John, A., Krummel, P. B., Luderer, G., Meinshausen, N., Montzka, S. A., Rayner, P. J., Reimann, S., Smith, S. J., van den Berg, M., Velders, G. J. M., Vollmer, M. K., and Wang, R. H. J.: The shared socio-economic pathway (SSP) greenhouse gas concentrations and their extensions to 2500, *Geosci. Model Dev.*, 13, 3571–3605, <https://doi.org/10.5194/gmd-13-3571-2020>, 2020.
- 1275 Metzger, S., Dentener, F., Pandis, S., and Lelieveld, J.: Gas/aerosol partitioning, 1, A computationally efficient model, *J. Geophys. Res.*, 107, 4312, doi:10.1029/2001JD001102, 2002.
- Monahan, E. C., and Muirchearthaigh, I.: Optimal power-law description of oceanic whitecap coverage dependence on wind speed, *J. Phys. Oceanogr.*, 10, 2094–2099, [https://doi.org/10.1175/1520-0485\(1980\)010<2094:OPLDOO>2.0.CO;2](https://doi.org/10.1175/1520-0485(1980)010<2094:OPLDOO>2.0.CO;2), 1980.
- Morales Betancourt, R. and Nenes, A.: Droplet activation parameterization: the population-splitting concept revisited, *Geosci. Model Dev.*, 7, 2345–2357, <https://doi.org/10.5194/gmd-7-2345-2014>, 2014.
- Morcrette, J.-J.: On the effects of the temporal and spatial sampling of radiation fields on the ECMWF forecasts and analyses, *Mon. Wea. Rev.*, 128, 876–887, [https://doi.org/10.1175/1520-0493\(2000\)128<0876:OTEOTT>2.0.CO;2](https://doi.org/10.1175/1520-0493(2000)128<0876:OTEOTT>2.0.CO;2), 2000.
- Morcrette, J.-J., Barker, H. W., Cole, J. N. S., Iacono, M. J., and Pincus, R.: Impact of a New Radiation Package, McRad, in the ECMWF Integrated Forecasting System. *Mon. Wea. Rev.*, 136, 4773–4798, <https://doi.org/10.1175/2008MWR2363.1>, 2008.
- 1285 Morcrette, J.-J., Boucher, O., Jones, L., Salmond, D., Bechtold, P., Beljaars, A., Benedetti, A., Bonet, A., Kaiser, J. W., Razinger, M., Schulz, M., Serrar, S., Simmons, A. J., Sofiev, M., Suttie, M., Tompkins, A. M., and Untch, A.: Aerosol analysis and forecast in the European Centre for Medium-Range Weather Forecasts Integrated Forecast System: Forward modeling, *J. Geophys. Res.*, 114, D06206, doi:10.1029/2008JD011235, 2009.
- 1290 Myriokefalitakis, S., Daskalakis, N., Gkouvousis, A., Hilboll, A., van Noije, T., Williams, J. E., Le Sager, P., Huijnen, V., Houweling, S., Bergman, T., Nüß, J. R., Vrekoussis, M., Kanakidou, M., and Krol, M. C.: Description and evaluation of a detailed gas-phase chemistry scheme in the TM5-MP global chemistry transport model (r112), *Geosci. Model Dev.*, 13, 5507–5548, <https://doi.org/10.5194/gmd-13-5507-2020>, 2020.
- 1295 Nakao, S., Tang, P., Tang, X., Clark, C. H., Qi, L., Seo, E., Asa-Awuku, A., and Cocker, D.: Density and elemental ratios of secondary organic aerosol: Application of a density prediction method, *Atmos. Environ.*, 68, 273–277, <https://doi.org/10.1016/j.atmosenv.2012.11.006>, 2013.
- van Noije, T. P. C., Le Sager, P., Segers, A. J., van Velthoven, P. F. J., Krol, M. C., Hazeleger, W., Williams, A. G., and Chambers, S. D.: Simulation of tropospheric chemistry and aerosols with the climate model EC-Earth, *Geosci. Model Dev.*, 7, 2435–2475, <https://doi.org/10.5194/gmd-7-2435-2014>, 2014.
- 1300 O'Neill, B. C., Tebaldi, C., van Vuuren, D. P., Eyring, V., Friedlingstein, P., Hurtt, G., Knutti, R., Kriegler, E., Lamarque, J.-F., Lowe, J., Meehl, G. A., Moss, R., Riahi, K., and Sanderson, B. M.: The Scenario Model Intercomparison Project (ScenarioMIP) for CMIP6, *Geosci. Model Dev.*, 9, 3461–3482, <https://doi.org/10.5194/gmd-9-3461-2016>, 2016.
- Ott, L. E., Pickering, K. E., Stenchikov, G. L., Allen, D. J., DeCaria, A. J., Ridley, B., Lin, R.-F., Lang, S., and Tao, W.-K.: Production of lightning NO_x and its vertical distribution calculated from three-dimensional cloud-scale chemical transport model simulations, *J. Geophys. Res.*, 115, D04301, doi:10.1029/2009JD011880, 2010.
- 1305 Ovadnevaite, J., Manders, A., de Leeuw, G., Ceburnis, D., Monahan, C., Partanen, A.-I., Korhonen, H., and O'Dowd, C. D.: A sea spray aerosol flux parameterization encapsulating wave state, *Atmos. Chem. Phys.*, 14, 1837–1852, <https://doi.org/10.5194/acp-14-1837-2014>, 2014.
- Parsons, L. A., Brennan, M. K., Wills, R. C. J., and Proistosescu, C.: Magnitudes and spatial patterns of interdecadal temperature variability in CMIP6. *Geophys. Res. Lett.*, 47, e2019GL086588, <https://doi.org/10.1029/2019GL086588>, 2020.



- 1310 Paasonen, P., Nieminen, T., Asmi, E., Manninen, H. E., Petäjä, T., Plass-Dülmer, C., Flentje, H., Birmili, W., Wiedensohler, A., Hörrak, U., Metzger, A., Hamed, A., Laaksonen, A., Facchini, M. C., Kerminen, V.-M., and Kulmala, M.: On the roles of sulphuric acid and low-volatility organic vapours in the initial steps of atmospheric new particle formation, *Atmos. Chem. Phys.*, 10, 11223–11242, <https://doi.org/10.5194/acp-10-11223-2010>, 2010.
- Perlwitz, J. P., Pérez García-Pando, C., and Miller, R. L.: Predicting the mineral composition of dust aerosols – Part 1: Representing key processes, *Atmos. Chem. Phys.*, 15, 11593–11627, <https://doi.org/10.5194/acp-15-11593-2015>, 2015a.
- Perlwitz, J. P., Pérez García-Pando, C., and Miller, R. L.: Predicting the mineral composition of dust aerosols – Part 2: Model evaluation and identification of key processes with observations, *Atmos. Chem. Phys.*, 15, 11629–11652, <https://doi.org/10.5194/acp-15-11629-2015>, 2015b.
- 1320 Pérez García-Pando, C., Miller, R. L., Perlwitz, J. P., Rodríguez, S., and Prospero, J. M.: Predicting the mineral composition of dust aerosols: Insights from elemental composition measured at the Izaña Observatory, *Geophys. Res. Lett.*, 43, 10520–10529, doi:10.1002/2016GL069873, 2016.
- Pincus, R., Forster, P. M., and Stevens, B.: The Radiative Forcing Model Intercomparison Project (RFMIP): experimental protocol for CMIP6, *Geosci. Model Dev.*, 9, 3447–3460, <https://doi.org/10.5194/gmd-9-3447-2016>, 2016.
- 1325 Price, C., and Rind, D.: Possible implications of global climate change on global lightning distributions and frequencies, *J. Geophys. Res.*, 99, 10823–10831, doi:10.1029/94JD00019, 1994.
- Prigent, C., Tegen, I., Aires, F., Marticorena, B., and Zribi, M.: Estimation of the aerodynamic roughness length in arid and semi-arid regions over the globe with the ERS scatterometer, *J. Geophys. Res.*, 110, D09205, doi:10.1029/2004JD005370, 2005.
- Ramankutty, N., and Foley, J. A.: Estimating historical changes in global land cover: Croplands from 1700 to 1992, *Global Biogeochem. Cycles*, 13, 997–1027, doi:10.1029/1999GB900046, 1999.
- 1330 Reid, J. S., Koppmann, R., Eck, T. F., and Eleuterio, D. P.: A review of biomass burning emissions part II: intensive physical properties of biomass burning particles, *Atmos. Chem. Phys.*, 5, 799–825, <https://doi.org/10.5194/acp-5-799-2005>, 2005.
- Riccobono F., Schobesberger S., Scott C. E., et al.: Oxidation products of biogenic emissions contribute to nucleation of atmospheric particles. *Science*. 344, 717–721, doi:10.1126/science.1243527, 2014.
- Ridley, B. A., Pickering, K. E., Dye, J. E.: Comments on the parameterization of lightning-produced NO in global chemistry-transport models, *Atmos. Environ.*, 39, 6184–6187, <https://doi.org/10.1016/j.atmosenv.2005.06.054>, 2005.
- 1335 Rotstayn, L. D., and Penner, J. E.: Indirect aerosol forcing, quasi forcing, and climate response, *J. Clim.*, 14, 2960–2975, 2001.
- Rousset, C., Vancoppenolle, M., Madec, G., Fichet, T., Flavoni, S., Barthélemy, A., Benshila, R., Chanut, J., Levy, C., Masson, S., and Vivier, F.: The Louvain-La-Neuve sea ice model LIM3.6: global and regional capabilities, *Geosci. Model Dev.*, 8, 2991–3005, <https://doi.org/10.5194/gmd-8-2991-2015>, 2015.
- 1340 Salter, M. E., Nilsson, E. D., Butcher, A., and Bilde, M.: On the seawater temperature dependence of the sea spray aerosol generated by a continuous plunging jet, *J. Geophys. Res. Atmos.*, 119, 9052–9072, doi:10.1002/2013JD021376, 2014.
- 1345 Salter, M. E., Zieger, P., Acosta Navarro, J. C., Grythe, H., Kirkevåg, A., Rosati, B., Riipinen, I., and Nilsson, E. D.: An empirically derived inorganic sea spray source function incorporating sea surface temperature, *Atmos. Chem. Phys.*, 15, 11047–11066, <https://doi.org/10.5194/acp-15-11047-2015>, 2015.
- 1350 Schmid, O., Chand, D., Karg, E., Guyon, P., Frank, G. P., Swietlicki, E., and Andreae, M. O.: Derivation of the density and refractive index of organic matter and elemental carbon from closure between physical and chemical aerosol properties, *Environ. Sci. Technol.*, 43, 1166–1172, doi:10.1021/es800570p, 2009.
- Segelstein, D. J.: The complex refractive index of water, M.Sc. Thesis, University of Missouri-Kansas City, U. S., 167 pp., 1981.
- Segers, A., van Velthoven, P., Bregman, B., and Krol, M.: On the computation of mass fluxes for Eulerian transport models from spectral meteorological fields, in: *Proceedings of the International Conference on Computational Science*, edited by: Sloot, P. M. A., Tan, C. J. K., Dongarra, J. J., and Hoekstra, A. G., 21–24 April 2002, Amsterdam, Netherlands, Lecture Notes in Computer Science, 2330, Springer-Verlag, Berlin, Heidelberg, Germany, 767–776, 2002.



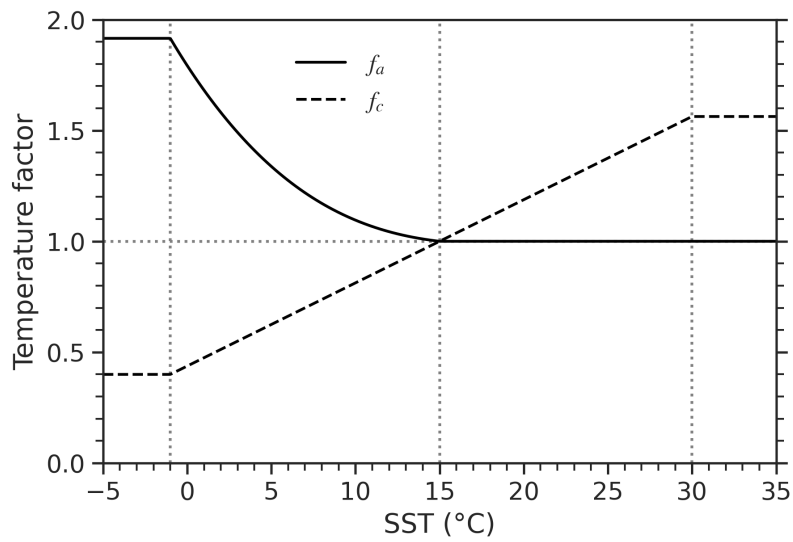
- 1360 Sherwood, S., Webb, M. J., Annan, J. D., Armour, K. C., Forster, P. M., Hargreaves, J. C., Hegerl, G., Klein, S. A., Marvel, K. D., Rohling, E. J., Watanabe, M., Andrews, T., Braconnot, P., Bretherton, C. S., Foster, G. L., Hausfather, Z., von der Heydt, A. S., Knutti, R., Mauritsen, T., Norris, J. R., Proistosescu, C., Rugenstein, M., Schmidt, G. A., Tokarska, K. B., and Zelinka, M. D.: An assessment of Earth's climate sensitivity using multiple lines of evidence, *Rev. Geophys.*, 58, e2019RG000678, <https://doi.org/10.1029/2019RG000678>, 2020.
- 1365 Sipilä, M., Berndt, T., Petäjä, T., Brus, D., Vanhanen, J., Stratmann, F., Patokoski, J., Mauldin III, R. L., Hyvärinen, A.-P., Lihavainen, H., and Kulmala, M.: The role of sulfuric acid in atmospheric nucleation, *Science*, 327, 1243–1246, doi:10.1126/science.1180315, 2010.
- 1370 Sindelarova, K., Granier, C., Bouarar, I., Guenther, A., Tilmes, S., Stavrou, T., Müller, J.-F., Kuhn, U., Stefani, P., and Knorr, W.: Global data set of biogenic VOC emissions calculated by the MEGAN model over the last 30 years, *Atmos. Chem. Phys.*, 14, 9317–9341, <https://doi.org/10.5194/acp-14-9317-2014>, 2014.
- Spahni, R., Wania, R., Neef, L., van Weele, M., Pison, I., Bousquet, P., Frankenberg, C., Foster, P. N., Joos, F., Prentice, I. C., and van Velthoven, P.: Constraining global methane emissions and uptake by ecosystems, *Biogeosciences*, 8, 1643–1665, <https://doi.org/10.5194/bg-8-1643-2011>, 2011.
- 1375 Sporre, M. K., Blichner, S. M., Schrödner, R., Karset, I. H. H., Berntsen, T. K., van Noije, T., Bergman, T., O'Donnell, D., and Makkonen, R.: Large difference in aerosol radiative effects from BVOC-SOA treatment in three Earth system models, *Atmos. Chem. Phys.*, 20, 8953–8973, <https://doi.org/10.5194/acp-20-8953-2020>, 2020.
- 1380 Stevens, B., Fiedler, S., Kinne, S., Peters, K., Rast, S., Müsse, J., Smith, S. J., and Mauritsen, T.: MACv2-SP: a parameterization of anthropogenic aerosol optical properties and an associated Twomey effect for use in CMIP6, *Geosci. Model Dev.*, 10, 433–452, <https://doi.org/10.5194/gmd-10-433-2017>, 2017.
- 1385 Stier, P., Feichter, J., Kinne, S., Kloster, S., Vignati, E., Wilson, J., Ganzeveld, L., Tegen, I., Werner, M., Balkanski, Y., Schulz, M., Boucher, O., Minikin, A., and Petzold, A.: The aerosol-climate model ECHAM5-HAM, *Atmos. Chem. Phys.*, 5, 1125–1156, <https://doi.org/10.5194/acp-5-1125-2005>, 2005.
- Stokes, R. H. and Robinson R. A.: Interactions in aqueous nonelectrolyte solutions. I. Solute-solvent equilibria, *J. Phys. Chem.*, 70, 2126 – 2131, <https://doi.org/10.1021/j100879a010>, 1966.
- 1390 Sundqvist, H.: A parameterization scheme for non-convective condensation including prediction of cloud water content, *Q. J. R. Meteorol. Soc.*, 104, 677–690, <https://doi.org/10.1002/qj.49710444110>, 1978.
- 1395 Tegen, I., Harrison, S. P., Kohfeld, K., Prentice, I. C., Coe, M., and Heimann, M.: Impact of vegetation and preferential source areas on global dust aerosol: Results from a model study, *J. Geophys. Res.*, 107, 4576, doi:10.1029/2001JD000963, 2002.
- Tegen, I., Werner, M., Harrison, S. P., and Kohfeld, K. E.: Relative importance of climate and land use in determining present and future global soil dust emission, *Geophys. Res. Lett.*, 31, L05105, doi:10.1029/2003GL019216, 2004.
- 1400 Tsigaridis, K., Daskalakis, N., Kanakidou, M., Adams, P. J., Artaxo, P., Bahadur, R., Balkanski, Y., Bauer, S. E., Bellouin, N., Benedetti, A., Bergman, T., Berntsen, T. K., Beukes, J. P., Bian, H., Carslaw, K. S., Chin, M., Curci, G., Diehl, T., Easter, R. C., Ghan, S. J., Gong, S. L., Hodzic, A., Hoyle, C. R., Iversen, T., Jathar, S., Jimenez, J. L., Kaiser, J. W., Kirkevåg, A., Koch, D., Kokkola, H., Lee, Y. H., Lin, G., Liu, X., Luo, G., Ma, X., Mann, G. W., Mihalopoulos, N., Morcrette, J.-J., Müller, J.-F., Myhre, G., Myriokefalitakis, S., Ng, N. L., O'Donnell, D., Penner, J. E., Pozzoli, L., Pringle, K. J., Russell, L. M., Schulz, M., Sciare, J., Seland, Ø., Shindell, D. T., Sillman, S., Skeie, R. B., Spracklen, D., Stavrou, T., Steenrod, S. D., Takemura, T., Tiitta, P., Tilmes, S., Tost, H., van Noije, T., van Zyl, P. G., von Salzen, K., Yu, F., Wang, Z., Wang, Z., Zaveri, R. A., Zhang, H., Zhang, K., Zhang, Q., and Zhang, X.: The AeroCom evaluation and intercomparison of organic aerosol in global models, *Atmos. Chem. Phys.*, 14, 10845–10895, <https://doi.org/10.5194/acp-14-10845-2014>, 2014.
- 1410 Turpin, B. J., and Lim, H.-J.: Species contributions to PM_{2.5} mass concentrations: Revisiting common assumptions for estimating organic mass, *Aerosol Sci. Technol.*, 35, 602–610, <https://doi.org/10.1080/02786820119445>, 2001.
- Twomey, S.: The influence of pollution on the shortwave albedo of clouds. *J. Atmos. Sci.*, 34, 1149–1152, [https://doi.org/10.1175/1520-0469\(1977\)034<1149:TlOPOT>2.0.CO;2](https://doi.org/10.1175/1520-0469(1977)034<1149:TlOPOT>2.0.CO;2), 1977.
- 1415 Vancoppenolle, M., Fichet, T., Goosse, H., Bouillon, S., Madec, G., Morales Maqueda, M. A.: Ocean Modelling, 27, 33–53, <https://doi.org/10.1016/j.ocemod.2008.10.005>, 2009.



- 1420 Vehkamäki, H., Kulmala, M., Napari, I., Lehtinen, K. E. J., Timmreck, C., Noppel, M., and Laaksonen, A.: An improved parameterization for sulfuric acid–water nucleation rates for tropospheric and stratospheric conditions, *J. Geophys. Res.*, 107, 4622, doi:10.1029/2002JD002184, 2002.
- Vignati, E., Wilson, J., and Stier, P.: M7: An efficient size-resolved aerosol microphysics module for large-scale aerosol transport models, *J. Geophys. Res.*, 109, D22202, doi:10.1029/2003JD004485, 2004.
- 1425 Vignati, E., Facchini, M. C., Rinaldi, M., Scannell, C., Ceburnis, D., Sciare, J., Kanakidou, M., Myriokefalitakis, S., Dentener, F., O'Dowd, C. D.: Global scale emission and distribution of sea-spray aerosol: Sea-salt and organic enrichment, *Atmos. Environ.*, 44, 670–677, 2010a.
- 1430 Vignati, E., Karl, M., Krol, M., Wilson, J., Stier, P., and Cavalli, F.: Sources of uncertainties in modelling black carbon at the global scale, *Atmos. Chem. Phys.*, 10, 2595–2611, <https://doi.org/10.5194/acp-10-2595-2010>, 2010b.
- Wanninkhof, R.: Relationship between wind speed and gas exchange over the ocean revisited, *Limnol. Oceanogr. Methods*, 12, doi:10.4319/lom.2014.12.351, 2014.
- 1435 Weber, R. J., Marti, J. J., McMurry, P. H., Eisele, F. L., Tanner, D. J., and Jefferson, A.: Measured atmospheric new particle formation rates: implications for nucleation mechanisms, *Chem. Eng. Commun.*, 151, 53–64, doi:10.1080/00986449608936541, 1996.
- 1440 Williams, J. E., Boersma, K. F., Le Sager, P., and Verstraeten, W. W.: The high-resolution version of TM5-MP for optimized satellite retrievals: description and validation, *Geosci. Model Dev.*, 10, 721–750, <https://doi.org/10.5194/gmd-10-721-2017>, 2017.
- 1445 Williams, J. E., Landgraf, J., Bregman, A., and Walter, H. H.: A modified band approach for the accurate calculation of online photolysis rates in stratospheric-tropospheric Chemical Transport Models, *Atmos. Chem. Phys.*, 6, 4137–4161, <https://doi.org/10.5194/acp-6-4137-2006>, 2006.
- 1450 Williams, J. E., Strunk, A., Huijnen, V., and van Weele, M.: The application of the Modified Band Approach for the calculation of on-line photodissociation rate constants in TM5: implications for oxidative capacity, *Geosci. Model Dev.*, 5, 15–35, <https://doi.org/10.5194/gmd-5-15-2012>, 2012.
- Williams, J. E., van Velthoven, P. F. J., and Brenninkmeijer, C. A. M.: Quantifying the uncertainty in simulating global tropospheric composition due to the variability in global emission estimates of Biogenic Volatile Organic Compounds, *Atmos. Chem. Phys.*, 13, 2857–2891, <https://doi.org/10.5194/acp-13-2857-2013>, 2013.
- 1455 Winijkul, E., Yan, F., Lu, Z., Streets, D. G., Bond, T. C., Zhao, Y.: Size-resolved global emission inventory of primary particulate matter from energy-related combustion sources, *Atmos. Environ.*, 107, 137–147, <https://doi.org/10.1016/j.atmosenv.2015.02.037>, 2015.
- 1460 Wood, R.: Parametrization of the effect of drizzle upon the droplet effective radius in stratocumulus clouds, *Q. J. R. Meteorol. Soc.*, 126, 3309–3324, <https://doi.org/10.1002/qj.49712657015>, 2000.
- 1465 Wyser, K., van Noije, T., Yang, S., von Hardenberg, J., O'Donnell, D., and Döschner, R.: On the increased climate sensitivity in the EC-Earth model from CMIP5 to CMIP6, *Geosci. Model Dev.*, 13, 3465–3474, <https://doi.org/10.5194/gmd-13-3465-2020>, 2020.
- Yarwood, G., Rao, S., Yocke, M., and Whitten, G. Z.: Updates to the carbon bond chemical mechanism: CB05. Final report to the U.S. Environmental Protection Agency, RT-0400675, 2005.
- 1470 Zdanovskii, A. B.: New methods for calculating solubilities of electrolytes in multicomponent systems, *Zh. Fiz. Khim.*, 22, 1475–1485, 1948.
- Zeleznik, F. J.: Thermodynamic properties of the aqueous sulfuric acid system to 350 K, *J. Phys. Chem. Ref. Data*, 20, 1157–1200, 1991.



- 1475 Zhang, K., O'Donnell, D., Kazil, J., Stier, P., Kinne, S., Lohmann, U., Ferrachat, S., Croft, B., Quaas, J., Wan, H., Rast, S., and Feichter, J.: The global aerosol-climate model ECHAM-HAM, version 2: sensitivity to improvements in process representations, *Atmos. Chem. Phys.*, 12, 8911–8949, <https://doi.org/10.5194/acp-12-8911-2012>, 2012.



1480 Figure 1: Temperature factors f_a and f_c for the formation of sea-spray particles in the accumulation and coarse mode, respectively.

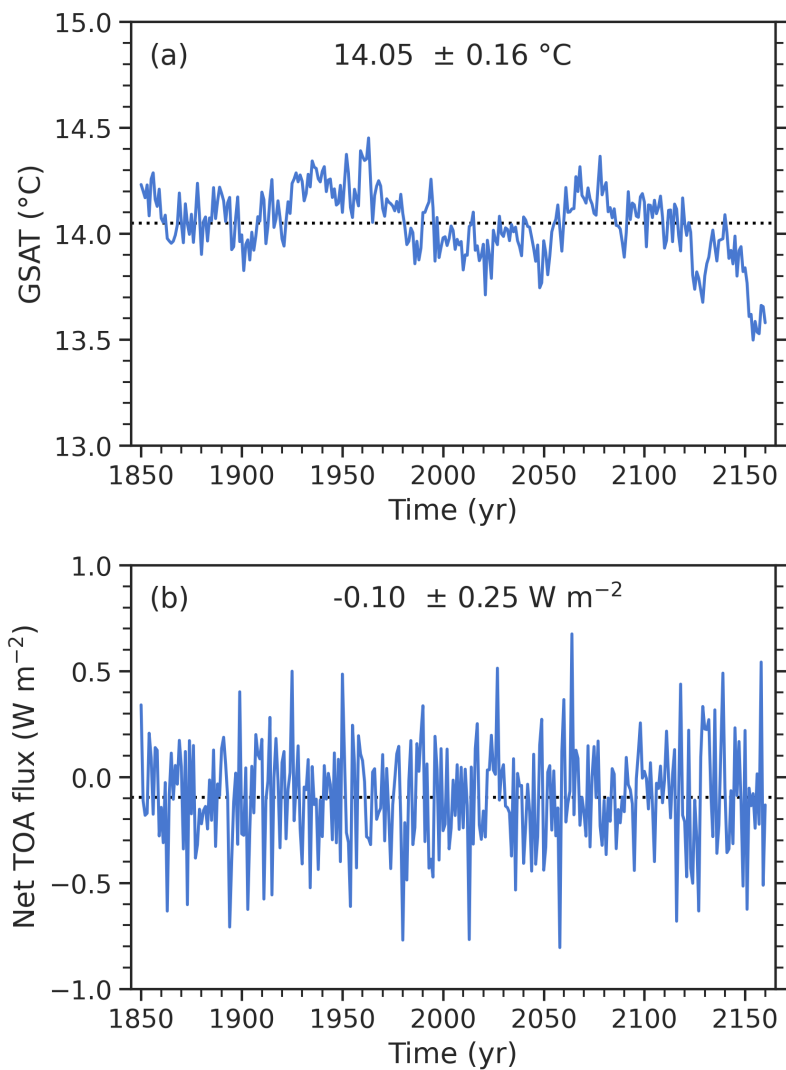
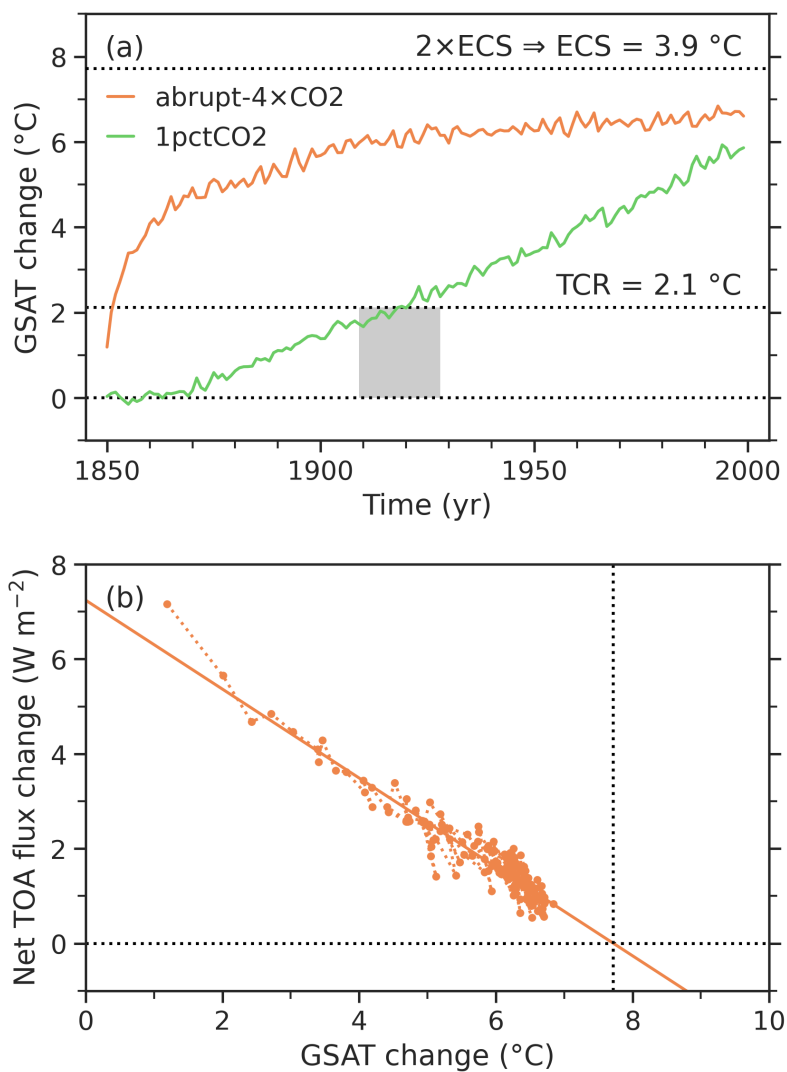


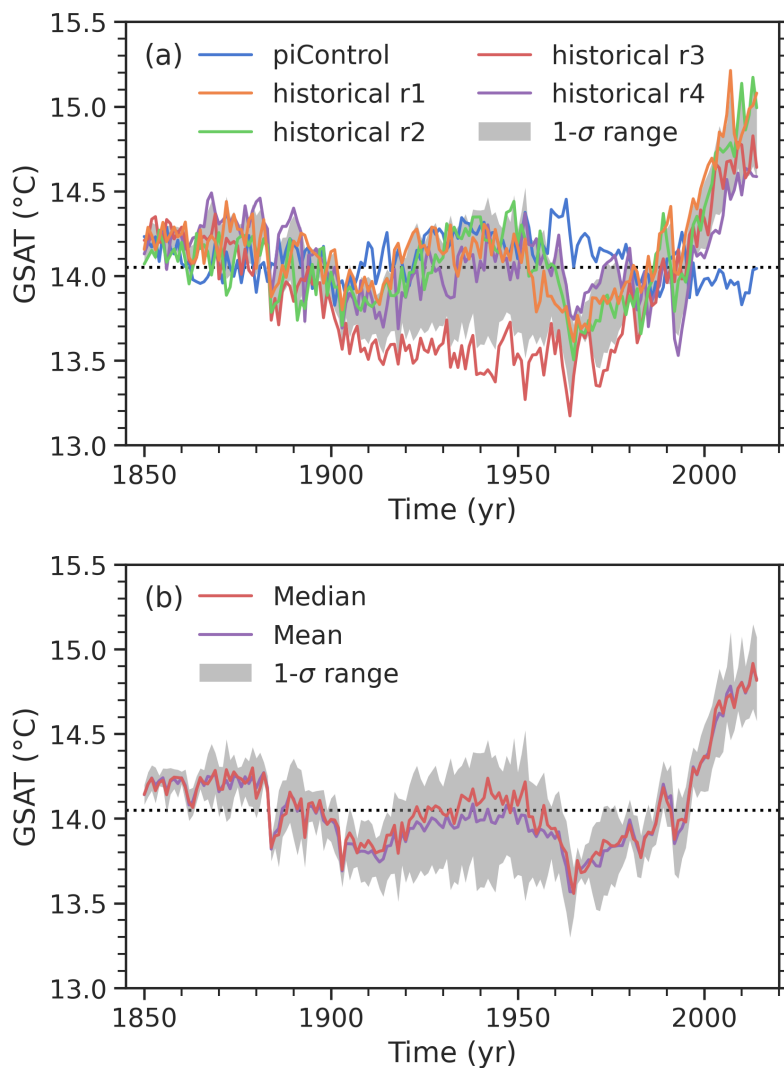
Figure 2: Time series of (a) the global surface air temperature (GSAT) and (b) the net radiative flux at the top of the atmosphere (TOA) in the pre-industrial control simulation (piControl). Shown are the annual mean values, and the corresponding means and standard deviations.

1485

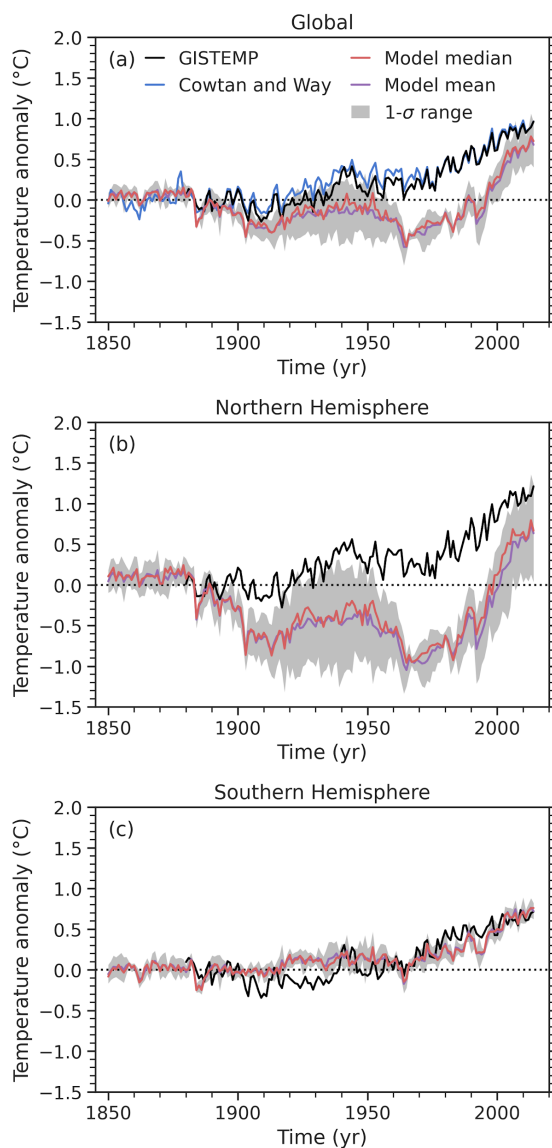


1490

Figure 3: (a) GSAT change in the simulation with abrupt quadrupling of CO₂ concentrations (abrupt-4×CO₂) and the simulation with a 1 percent CO₂ concentration increase per year (1pctCO₂); (b) Net radiative flux change at the top of the atmosphere versus GSAT change in the abrupt-4×CO₂ experiment, together with a linear fit obtained by Theil-Sen regression. The temperature and flux changes shown in this figure are the annual mean deviations from the linear trend lines through the corresponding 150 years of the pre-industrial control simulation.

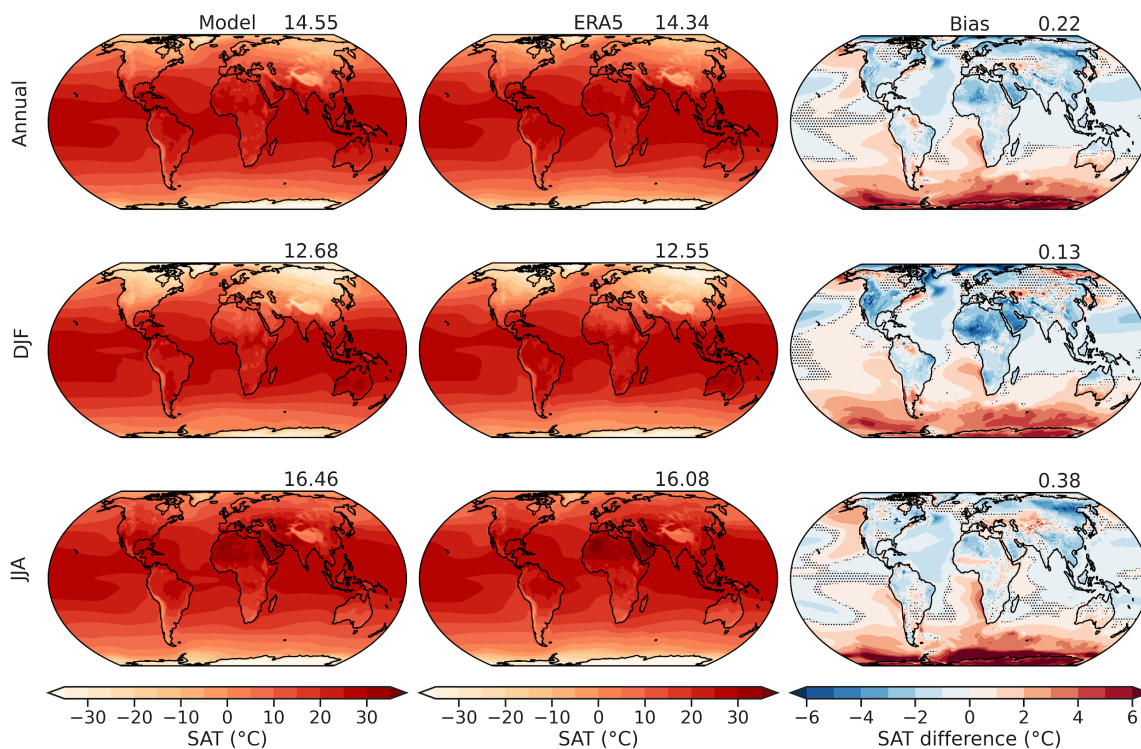


1495 **Figure 4:** Time series of the annual and global mean surface air temperature for the four realizations of the CMIP6 historical simulation (a), and the corresponding ensemble median and mean values (b). In both panels, the grey area indicates the range bounded by one standard deviation around the ensemble mean, and the dotted line indicates the pre-industrial mean of 14.05 °C. For comparison, panel (a) also shows the corresponding time series for the first 165 years of the pre-industrial control simulation.

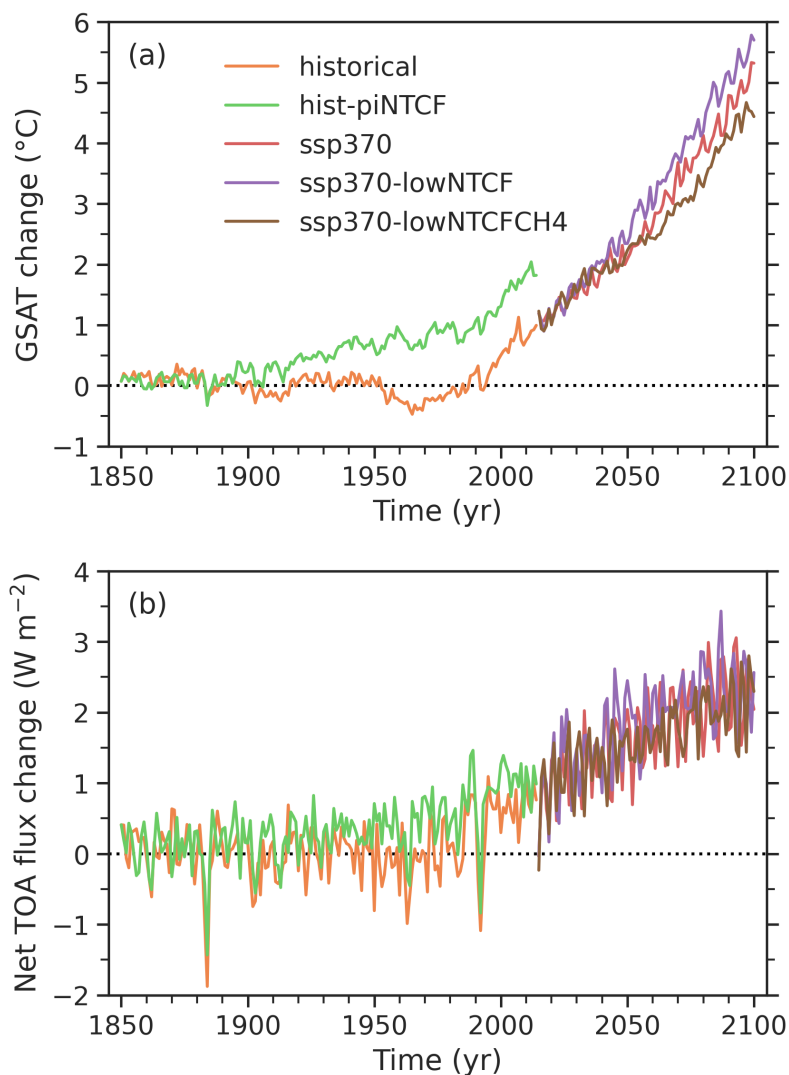


1500

Figure 5: The median, mean and one-standard deviation range of the annual mean surface air temperature (SAT) anomalies from the four realizations of the CMIP6 historical simulation compared to reconstructed surface temperature anomalies from GISTEMP version 4 and HadCRUT4 infilled by kriging (Cowtan and Way version 2.0). The anomalies are defined with respect to the period 1850–1900 (1880–1900 for GISTEMP). Panels (a), (b) and (c) show the global, Northern Hemisphere, and Southern Hemisphere means, respectively.



1505 **Figure 6:** Surface air temperature (SAT) climatology for the years 1995–2014 from the four-member ensemble of the CMIP6 historical simulation and the ERA5 reanalysis (version 2), and the corresponding differences. The top row shows the full multi-annual means, the middle and bottom rows the means for boreal winter (December, January, February; DJF) and summer (June, July, August; JJA), respectively. The number given at the top right of each panel is the global mean value. The stippled areas in the panels on the right indicate the regions where the differences are not significant at the 5 % level.



1510 **Figure 7: Change in (a) the global surface air temperature (GSAT) and (b) the net TOA flux in the CMIP6 historical simulation, the**
AerChemMIP historical simulation with emissions of near-term climate forcers (NTCFs) fixed to pre-industrial levels (hist-piNTCF),
and future simulations for the standard SSP3-7.0 scenario, a corresponding scenario with low NTCF emissions (SSP3-7.0-lowNTCF),
and a corresponding scenario with both low NTCF emissions and low CH₄ concentrations (SSP3-7.0-lowNTCFCH₄). The temperature
1515 **and flux changes shown in this figure are the annual mean deviations from the pre-industrial means given in Fig. 2. Only the first**
ensemble member (r1i1p1f1) of each experiment is presented.

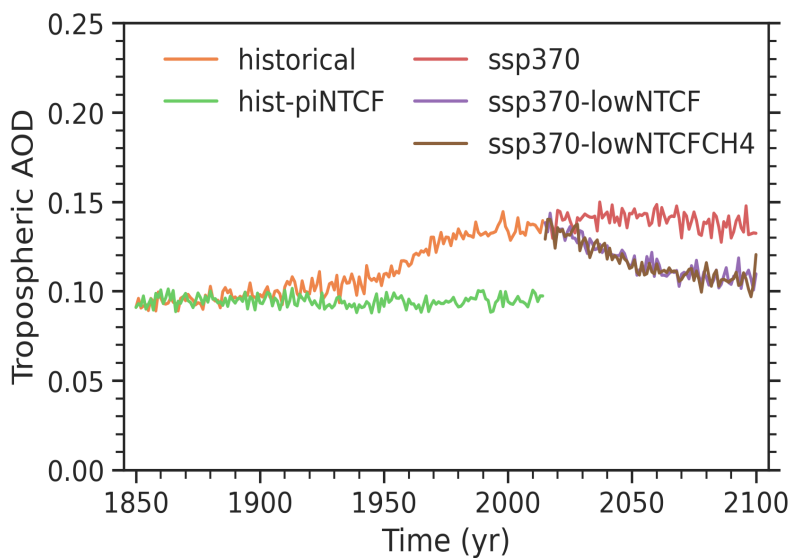


Figure 8: Annual global mean tropospheric aerosols optical depth (AOD) at 550 nm in the simulations presented in Fig. 7.